CrossMark

J. Fluid Mech. (2016), *vol.* 790, *pp.* 205–236. © Cambridge University Press 2016
doi:10.1017/jfm.2016.9

Axisymmetric outflows from binary point-source systems in the presence of an interface

Lawrence K. Forbes†

School of Mathematics and Physics, University of Tasmania, Box 37, Hobart 7001, Australia

(Received 5 June 2015; revised 15 October 2015; accepted 4 January 2016;
first published online 2 February 2016)

Fluid outflow is considered, from a binary system of two point sources. The sources inject fluid of a lower density than the surrounding medium, and there is a sharp interface separating the two fluids. The overall geometry is taken to be axisymmetric around the line joining the two sources. Numerical solutions are presented for the shape of the interface in unsteady flow, and compared with a linearized solution based on small deformation of the interface from its initial spherical configuration. In addition, a novel spectral method is developed for the solution of the Boussinesq viscous flow problem, accounting exactly for the presence of the two sources and modelling the interface as a narrow region in which fluid mixing is possible. Bipolar outflow jets are seen to be possible.

Key words: computational methods, geophysical and geological flows, stratified flows

1. Introduction

Perhaps the simplest problem to formulate in free-surface hydrodynamics is to find the shape of an interface or free surface that is distorted by the presence of a single point source or line source. However, while easy to pose, the problem is remarkably difficult to solve, and perhaps deserves to be regarded as a canonical problem in the subject. Earlier work ignored time-dependent effects and solved the steady-state problem in purely inviscid fluid. This creates an unexpected difficulty, however, since there is no natural linearization possible in the steady case, so that the problem is fundamentally nonlinear. Peregrine (1972) studied planar outflow from a line source beneath a free surface, using an expansion in powers of the square of the source strength, and estimated a maximum strength at which the free surface might form a stagnation point, so that in a time-dependent situation, wave breaking might then occur. Later, however, Vanden-Broeck, Schwartz & Tuck (1978) showed that expansions in powers of the Froude number are formally asymptotic only, having zero radius of convergence, and Peregrine's expansion is indeed one of this type. Tuck & Vanden-Broeck (1984) devised an ingenious spectral-type method based on the use of complex variables, and they used it to compute an isolated steady solution at a unique value of the source strength (Froude number). Their solution possessed a downward-pointing cusp directed at the line source (or sink) below the free surface, and it has been speculated by Hocking (1995) and others that such a solution might represent the

† Email address for correspondence: larry.forbes@utas.edu.au

https://doi.org/10.1017/jfm.2016.9 Published online by Cambridge University Press

source strength at which selective withdrawal begins, and the free surface (or interface) is drawn right into the sink.

Tuck & Vanden-Broeck's (1984) isolated solution occurs at a value of source strength considerably larger than the maximum value estimated by Peregrine (1972), so that there is an effective 'gap' in the source strength, in which steady-state solutions are apparently not possible. This has prompted a search for planar unsteady solutions in that parameter region, to explain this phenomenon. Stokes, Hocking & Forbes (2003) used a numerical method to solve the unsteady problem for a line sink beneath a free surface, and compared it with the results of a low-order expansion in time. Their results show that the behaviour of the solution in this 'gap' region of source strengths is sensitive to initial conditions, and may give breaking waves or a partial draw down of the interface, followed by a rebound. Broadly similar results had been obtained earlier for three-dimensional flows by Xue & Yue (1998), with a point sink beneath a free surface in axisymmetric flow. In addition to their academic interest, these studies of free-surface flows caused by a source in a horizontal layer of fluid have application in the management of reservoirs, where genuinely selective withdrawal from a single layer only may be desired Hocking (1995).

Interfacial outflows from sources in fluids are also possible in geometries other than the purely planar case, and may find application in astrophysics or the study of underwater explosions. In such systems, there are additional behaviour possibilities caused by the curvature of the interface itself, for which there is no equivalent in planar geometry. This is a result of the Bell–Plesset instability, which is discussed by Epstein (2004), and has a strong influence on the stability of the flow. Forbes (2011*a*) considered cylindrical outflow from a line source, in which a less dense fluid is injected into a heavier one, so that the overall flow was a type of cylindrical Rayleigh–Taylor problem. These cylindrical outflows are of relevance to situations arising in astrophysics, and Matsuoka & Nishihara (2006) have computed similar-looking solutions to those of Forbes (2011*a*), but produced by a Richtmyer–Meshkov instability arising from the interaction with a shock. It is found that, when the outer fluid is heavier than the inner one, so that a Rayleigh–Taylor type flow ensues, the outflow shape that is produced at the interface is strongly dependent on the initial disturbance to the cylindrical interface or the perturbation to the fluid velocity within it.

Forbes (2011*b*), however, showed that a very different situation exists for axisymmetric flow produced by a point source, enclosed initially by a spherical interface. A linearized solution in the case of inviscid flow demonstrates that the first Legendre mode is the most unstable one. This means that the eventual flow is not greatly sensitive to the initial perturbation, but rather that the first mode grows most rapidly and ultimately dominates. As a result, the flow becomes a one-sided jet, out of one of the poles of the initial sphere. This is a surprising outcome, but it is based on a linearized inviscid stability equation, that turns out to be identical to one derived earlier by Mikaelian (2005). Forbes (2011*b*) also carried out a nonlinear viscous solution numerically, and those results confirmed the presence of one-sided outflow jets from a single point source.

Numerically-generated solutions for outflows from astrophysical objects in the presence of magnetic fields have been carried out by Lovelace *et al.* (2010), and those complex situations also resulted in one-sided outflows. Furthermore, since the gravitational field is directed purely inwards towards the point source, there is no reason to suppose that the one-sided jet should prefer one pole of the sphere to the other, and indeed, their computations suggested that the outflow flipped from one pole

https://doi.org/10.1017/jfm.2016.9 Published online by Cambridge University Press

to the other on a reasonably regular time interval. This would be consistent with the linearized inviscid solution of Forbes (2011*b*), in spite of its relative simplicity in comparison to the simulations of Lovelace *et al.* (2010). Furthermore, such switching flows have been studied experimentally by Chené & St-Louis (2010), for a Wolf–Rayet star in astrophysics. More recent computations of asymmetric outflows from single stars have been presented by Lovelace *et al.* (2014) and confirm the presence of an asymmetric outflow that alternates from one side of the centre plane to the other. Careful observations of the Herbig–Haro star HH-111 over an interval of 15 years have been reported by Gómez, Rodríguez & Loinard (2013) and these show the formation of a one-sided jet from that object.

Nevertheless, astrophysics also provides many instances of strongly bipolar outflows from various objects, as is discussed in the text by Stahler & Palla (2004, chap. 13) and the review by Zinnecker & Yorke (2007). Several possible explanations present themselves, at least in the astrophysical context, and one obvious one might be the inclusion of magnetic effects, since these must impose a dipole pattern on the outflow geometry to some extent. However, Lovelace *et al.* (2014) found that asymmetric flows that switched from one pole to the other were still possible even with the inclusion of such effects. Recently, Forbes (2014*a*) sought to generate bipolar outflows by adding a straining flow in the outer fluid, and also by accounting for the effects of rotation. In a nonlinear viscous model, this did indeed lead to two-sided outflows, but they were not completely symmetrical about the centre plane. When the two fluids inside and outside the interface have very similar densities, Forbes & Brideson (2014) derived a nonlinear partial differential equation for the approximate shape of the interface in a straining flow, and showed that they could find exact closed-form solutions to their equation. These approximate shapes were bipolar and symmetric.

Another possibility for the generation of bipolar outflows is that two (or more) sources may be present in the fluid, instead of just one. This scenario is studied here, in order to determine the types of outflow that it can produce. Although a major interest in the phenomenon here is from the point of view of fundamental fluid mechanics, there is nevertheless significant evidence that it may again be relevant to observations undertaken in astrophysics. Ladd & Hodapp (1997) reported an apparent double outflow from within a molecular cloud, and postulated that it could be caused by two sources deeply embedded in that object. Ulvestad, Wrobel & Carilli (1999) used radio-astronomical measuring techniques to image a bright infrared galaxy and likewise found evidence that suggests the possibility of two, or perhaps three, sources in relatively close proximity. In a study of a quadrupolar outflow from a Herbig–Haro object, Franco-Hernández & Rodríguez (2003) detected the presence of a double source, and more recently, Forbrich *et al.* (2009) have also detected a separate binary system of protostars, having masses 3.5 and $1.2\,\mathrm{M}_{\odot}$ and producing two intersecting jets. Murphy *et al.* (2008) note that outflow from a system containing multiple protostars often involves only a single jet, and they undertook numerical simulation to account for the phenomenon. They conclude that the second jet is effectively absorbed into the main one, to the extent that it ceases to be readily visible. A similar result may be obtained in the present study, too, and such a case is discussed in § 5.

A truly fascinating instance of what appears to be interfacial outflow from a binary source system is evidently provided by the astrophysical object Eta Carinae, and this formed part of the initial motivation for undertaking the present work. This object has been the subject of intense study in the astrophysical literature, and a review of

https://doi.org/10.1017/jfm.2016.9 Published online by Cambridge University Press

work until about the end of the twentieth century is given by Davidson & Humphreys (1997). The system has an overall mass of perhaps 140 times that of our Sun, and is millions of times as luminous. In approximately 1844, it underwent a cataclysmic explosion, referred to as the 'Great Eruption', after which it became the second most bright star in the night sky for some years. During that time, it ejected in excess of $10\,\mathrm{M}_\odot$ of material, creating a 'Homunculus nebula' that surrounds the inner region and obscures its view. This nebula consists of dust and ejected gas, forming two large osculating spheres such that the overall structure is approximately axisymmetric. A model that accounts for some features of the 'Great Eruption' of 1844 has been advanced by Smith (2013), and further details about the bipolar homunculus nebula and its composition are given by Steffen *et al.* (2014). After some debate in the literature, the consensus is now that the Eta Carinae object most likely consists of two stars, one of about $110\,\mathrm{M}_\odot$ and the other of perhaps $30\,\mathrm{M}_\odot$. They rotate about each other in a highly eccentric orbit, and each continues to eject a large volume of gas (hadrons) into the surrounding medium. The interaction of these stellar winds is the subject of very recent work by Clementel *et al.* (2015). Fascinating recent work by Madura *et al.* (2015) has modelled outflow from these orbiting binary stars using code based on smoothed-particle hydrodynamics, and formatting the three-dimensional output of this simulation to a 3D-printer. A very recent NASA website (NASA 2015) offers an animated view into the centre of Eta Carinae, based on observations and hydrodynamic simulations of the type presented by Madura *et al.* (2015).

The present paper is a continuation of a sequence of investigations into fluid outflows from compact objects, and, motivated by astrophysical considerations, is focussed on the situation in which two point sources, located within a bubble of fluid of different density to its surrounds, are both ejecting mass. This is evidently the situation in an object such as Eta Carinae, where its two stars are ejecting hadrons into a more dense medium of dust and molecular hydrogen (Steffen *et al.* 2014). For simplicity, the two masses here are assumed to be stationary, allowing the simplifying approximation that the overall geometry is axisymmetric. Such a study may also be of interest in underwater explosions or in the injection of fluid into a reservoir, and so is of interest here also as a problem in fundamental fluid mechanics.

Since material ejected from the sources is of lower density than the surrounding fluid, the interface between them is subject to Rayleigh–Taylor instability. This type of flow is classical, and occurs when a horizontal layer of heavier fluid overlies a second layer of less dense fluid. The interface between them is unstable to small perturbations, which grow at a rate determined by the ratio of the densities of the two fluids. Forbes, Chen & Trenham (2007) developed a spectral solution technique for finding the evolving interface shape between layers of inviscid, incompressible fluid, and this was used by Forbes (2009) to study nonlinear interfacial influences on the growth of the interface in classical planar Rayleigh–Taylor flow. A later study of planar outflow from a line sink (Forbes 2011*a*) showed that, in this two-dimensional geometry, the initial conditions determined the shape that the interface would adopt at later times, although the initially cylindrical nature of the interface resulted in Bell–Plesset effects (Epstein 2004) due to its curvature, and these made stability considerations more complicated than just the Rayleigh–Taylor criterion. Initial conditions no longer determine the outflow shape in three-dimensional geometry, and Forbes (2011*b*) demonstrated that, instead, a one-sided jet is generated by outflow from a point source in the presence of an (initially spherical) interface. In a subsequent attempt to produce a two-sided, bipolar, outflow from a single point source in three-dimensional geometry, Forbes (2014*a*) included rotation and an

https://doi.org/10.1017/jfm.2016.9 Published online by Cambridge University Press

external straining flow field, and demonstrated that two-sided outflows could indeed be generated by these mechanisms.

The present research is therefore motivated by the desire to determine whether strongly bipolar outflows are likely to be the result of including two (or more) sources within the initial bubble of less dense fluid in three-dimensional geometry, similar to the situation believed to occur within the Eta Carinae object (Madura *et al.* 2015). For planar flows involving two line sources, Forbes (2014*b*) has shown that outflows containing two jets do occur, but this gives no indication of the likely outflow morphology when two point sources in three-dimensional geometry are responsible for the flow. This question is addressed here for an initially spherical inner region of less dense fluid, in both the inviscid and a (Boussinesq) viscous model of the situation.

To begin, an inviscid, incompressible model of axisymmetric outflow from two point sources in an unbounded fluid system is first described. The sources emit fluid at some reference density into an outer fluid of different density, such that the two fluids are initially separated by a spherical surface. A method for the solution of this problem is developed in § 2, and is an extension of the spectral solution technique advanced by Forbes *et al.* (2007). A linearized theory is also possible in the inviscid case, assuming only small perturbations about the initially spherical shape of the interface, and gives a useful check on the reliability of the nonlinear results. This is described in § 3.

The effects of viscosity on these binary outflows are also included, and the viscous approach is outlined in § 4, using a Boussinesq approximation. A second aim of this paper is to develop a spectral solution technique for viscous fluids, that is capable of dealing exactly with the presence of two (or more) point singularities within the fluid, and the method for achieving this is outlined in § 4. Results are discussed in § 5, and they show that bipolar outflows are indeed possible, depending on the choice of parameters in the problem. One-sided jets are nevertheless still possible in this three-dimensional geometry, and they may develop 'knots' along their lengths. A brief discussion concludes the paper in § 6.

2. Inviscid fluid model

Consider a system of two fluids of different densities. An inner fluid of some finite volume sits in an initially spherical region of radius a centred at the origin of a Cartesian coordinate system. This inner fluid has density ρ_1. It is enclosed within a second fluid of unbounded extent, and having density ρ_2. There is a sharp interface between these two fluids, across which the fluids are not free to mix.

Two heavy masses are present within the sphere of inner fluid 1 with density ρ_1, and each has its own gravitational field. Mass number 1 is located at the point $(0, 0, B)$ on the z-axis and has mass M_1. Furthermore, it ejects fluid of the same density ρ_1 isotropically at the volume flow rate m_1. The second mass is also on the z-axis at the opposite point $(0, 0, -B)$, with $B < a$. This incurs no loss of generality, since the coordinate system can always be rotated and translated to ensure this is the case. This second object has mass M_2 and emits fluid of density ρ_1 at the rate m_2 (volume per time). Both fluids are assumed in this section to be incompressible and inviscid, so that they flow irrotationally.

Following Forbes (2011*b*, 2014*a*), the problem is now recast in terms of spherical polar coordinates (r, ϕ, θ), in which r is the radial distance from the origin, ϕ is the declination angle down from the z-axis and θ is the azimuthal angle in the xy-plane

https://doi.org/10.1017/jfm.2016.9 Published online by Cambridge University Press

around the z-axis. The relation between these and Cartesian coordinates is expressed in the usual formulae

$$\left.\begin{aligned} x &= r\sin\phi\cos\theta, \quad 0<r<\infty,\\ y &= r\sin\phi\sin\theta, \quad 0<\phi<\pi,\\ z &= r\cos\phi, \quad -\pi<\theta<\pi, \end{aligned}\right\} \tag{2.1}$$

which are given in Kreyszig (2011, p. 594). Now the first mass is located at the point $(r,\phi)=(B,0)$ and the second mass has position $(r,\phi)=(B,\pi)$ independently of θ. The fluid velocity vector is written $\boldsymbol{q}=u\boldsymbol{e}_r+w\boldsymbol{e}_\phi+v\boldsymbol{e}_\theta$, where the three unit vectors $\boldsymbol{e}_r$, $\boldsymbol{e}_\phi$ and $\boldsymbol{e}_\theta$ point in the r, ϕ and θ-directions, respectively. In this paper, the flow will be assumed to be axisymmetric, so that there is no dependence on the coordinate θ. In addition the azimuthal velocity component is taken to be zero; $v=0$.

Non-dimensional coordinates are defined, and are used throughout this paper. The length scale is taken to be the initial radius a of the sphere. An arbitrary reference flow rate m_R (volume per time) is chosen, and then the time scale is a^3/m_R and the scale for speed becomes m_R/a^2. Pressures are then scaled relative to the quantity $\rho_1 m_R^2/a^4$, in which ρ_1 is the density in inner fluid 1. Velocity potential and streamfunction are both made dimensionless by reference to the quantity m_R/a. Notice that, since the reference volume flow rate m_R is arbitrary, it could be set to either of the quantities m_1 or m_2 already present in this problem, so eliminating the need for one of the dimensionless constants arising. However, it is preferable to allow the reference quantity m_R to remain genuinely arbitrary, since this allows an obvious linearized solution to be developed, as outlined in § 3. This form of the non-dimensionalization now naturally leads to the presence of the six dimensionless constants

$$\left.\begin{aligned} F_1 &= \frac{m_R}{\sqrt{GM_1a^3}}; \quad \beta=\frac{B}{a}; \quad \gamma=\frac{M_2}{M_1},\\ D &= \frac{\rho_2}{\rho_1}; \quad \eta_1=\frac{m_1}{m_R}; \quad \eta_2=\frac{m_2}{m_R}. \end{aligned}\right\} \tag{2.2}$$

The first of these constants F_1 may be regarded as a Froude number based on the mass M_1 of the (upper) source, and G in this expression is the gravitational constant. The quantity β is now the dimensionless distance of each mass from the origin, and since these masses lie within the initial sphere of dimensionless radius 1 containing the inner fluid, it follows that $\beta<1$. The ratio of the two masses is γ, and D is the density ratio of the outer fluid to the inner one. Finally, the two dimensionless outflow strengths from the two masses are η_1 and η_2. These quantities could be either negative or positive, depending on whether these objects behave as sources or sinks. A sketch of the dimensionless flow situation is given in figure 1.

Since the two fluids are modelled in this section as being inviscid, they flow without rotation. Consequently, the velocity vector in the inner fluid may be written $\boldsymbol{q}_1=\nabla\Phi_1$ and similarly, $\boldsymbol{q}_2=\nabla\Phi_2$ for the fluid in the surrounding medium. The two functions Φ_1 and Φ_2 are velocity potentials in the inner and outer fluids, respectively. As each fluid is incompressible, it follows that each velocity potential satisfies Laplace's equation $\nabla^2\Phi_j=0$, $j=1,2$ in its appropriate fluid domain. In inner fluid 1, there are two sources, and each of these is modelled as a mathematical point singularity for convenience. As a result, the velocity potential Φ_1 near the top source must behave as

$$\Phi_1 \to -\frac{\eta_1}{4\pi\sqrt{r^2-2\beta r\cos\phi+\beta^2}} \quad \text{as } (r,\phi)\to(\beta,0). \tag{2.3}$$

https://doi.org/10.1017/jfm.2016.9 Published online by Cambridge University Press

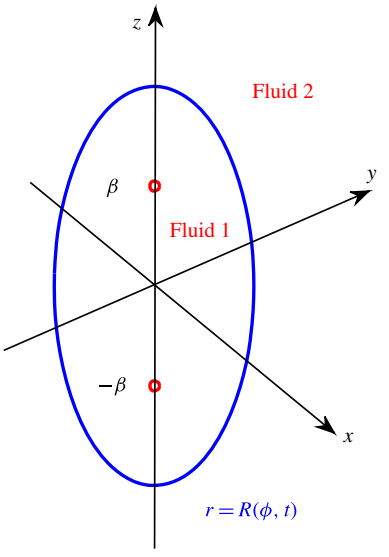


FIGURE 1. (Colour online) A sketch of the dimensionless configuration for the inviscid outflow from the two sources.

Similarly, near the bottom source,

$$\Phi_1 \to -\frac{\eta_2}{4\pi\sqrt{r^2+2\beta r\cos\phi+\beta^2}} \quad \text{as } (r,\phi)\to(\beta,\pi). \tag{2.4}$$

Between the two fluids, there is assumed to be an infinitesimally thin interface with the equation $r=\mathscr{R}(\phi,t)$, as illustrated in figure 1. The fluid on each side of the interface does not cross it, and this is expressed by the two kinematic boundary conditions

$$u_j=\frac{\partial\mathscr{R}}{\partial t}+\frac{w_j}{\mathscr{R}}\frac{\partial\mathscr{R}}{\partial\phi} \quad \text{on } r=\mathscr{R}(\phi,t), j=1,2 \tag{2.5}$$

at the interface. It is also necessary to impose a dynamical condition that the pressures either side of this interface must be equal. In each fluid, the pressure may be calculated from Bernoulli's equation, which is a first integral of the Euler equations of motion (see Batchelor 1967, § 3.5), and equating these pressures gives

$$\begin{aligned} &D\frac{\partial\Phi_2}{\partial t}-\frac{\partial\Phi_1}{\partial t}+\frac{1}{2}D(u_2^2+w_2^2)-\frac{1}{2}(u_1^2+w_1^2)\\ &\quad-\frac{(D-1)}{F_1^2}\left[\frac{1}{\sqrt{r^2-2\beta r\cos\phi+\beta^2}}+\frac{\gamma}{\sqrt{r^2+2\beta r\cos\phi+\beta^2}}\right]\\ &\quad=f(t) \quad \text{on } r=\mathscr{R}(\phi,t). \end{aligned} \tag{2.6}$$

Here, the function $f(t)$ is arbitrary, and has no effect on the interface shape.

https://doi.org/10.1017/jfm.2016.9 Published online by Cambridge University Press

It follows (from separation of variables arguments) that velocity potentials in the two fluids may be written

$$\Phi_1(r,\phi,t) = -\frac{\eta_1}{4\pi\sqrt{r^2-2\beta r\cos\phi+\beta^2}} - \frac{\eta_2}{4\pi\sqrt{r^2+2\beta r\cos\phi+\beta^2}} + \sum_{n=1}^{N} B_n(t) r^n P_n(\cos\phi) \tag{2.7}$$

and

$$\Phi_2(r,\phi,t) = -\frac{\eta_1}{4\pi\sqrt{r^2-2\beta r\cos\phi+\beta^2}} - \frac{\eta_2}{4\pi\sqrt{r^2+2\beta r\cos\phi+\beta^2}} + \sum_{n=1}^{N} C_n(t) r^{-n-1} P_n(\cos\phi). \tag{2.8}$$

These expressions become exact as the number of modes N becomes infinite; however, numerical considerations require a finite value for N. The unknown coefficient functions $B_n(t)$ and $C_n(t)$ are to be found. The interface shape is similarly expressed in the form

$$\mathscr{R}(\phi,t) = A(t) + H_0(t) + \sum_{n=1}^{N} H_n(t) P_n(\cos\phi). \tag{2.9}$$

The functions $P_n(z)$ in these expressions (2.7)–(2.9) are Legendre polynomials, as presented in Gradshteyn & Ryzhik (2000, § 8.91). These polynomials and their derivatives may be generated efficiently from their three-term recurrence formulae, which are presented in Forbes (2011*b*) for these spherical coordinates. The coefficients $H_0(t)$ and $H_n(t)$, $n = 1, \ldots, N$, in (2.9) are to be determined, but the average time-dependent outflow radius has the known value

$$A(t) = \left[1 + \frac{3(\eta_1+\eta_2)t}{4\pi}\right]^{1/3}, \tag{2.10}$$

which follows purely from considerations of mass balance. The series (2.7), (2.8) satisfy Laplace's equation in their respective domains, and (2.7) also satisfies the singular behaviours (2.3), (2.4) near the two sources in the inner layer.

The unknown coefficient functions in (2.7)–(2.9) are determined using the first 'basic' solution scheme presented by Forbes *et al.* (2007). To begin, velocity components $U_1(\phi,t)$, $W_1(\phi,t)$ and $U_2(\phi,t)$, $W_2(\phi,t)$ are defined on the actual moving interface $r = \mathscr{R}(\phi,t)$ itself, by taking the vector gradients of the two potentials Φ_1 and Φ_2 in (2.7) and (2.8). Thus

$$\begin{aligned} U_1(\phi,t) &= \left.\frac{\partial\Phi_1}{\partial r}\right|_{r=\mathscr{R}} \\ &= \frac{\eta_1(\mathscr{R}-\beta\cos\phi)}{4\pi[\mathscr{R}^2-2\beta\mathscr{R}\cos\phi+\beta^2]^{3/2}} + \frac{\eta_2(\mathscr{R}+\beta\cos\phi)}{4\pi[\mathscr{R}^2+2\beta\mathscr{R}\cos\phi+\beta^2]^{3/2}} \\ &\quad + \sum_{n=1}^{N} nB_n(t)\mathscr{R}^{n-1}P_n(\cos\phi) \end{aligned} \tag{2.11}$$

https://doi.org/10.1017/jfm.2016.9 Published online by Cambridge University Press

and

$$W_1(\phi,t) = \frac{1}{r}\frac{\partial \Phi_1}{\partial \phi}\bigg|_{r=\mathscr{R}}$$
$$= \frac{\eta_1\beta\sin\phi}{4\pi[\mathscr{R}^2-2\beta\mathscr{R}\cos\phi+\beta^2]^{3/2}} - \frac{\eta_2\beta\sin\phi}{4\pi[\mathscr{R}^2+2\beta\mathscr{R}\cos\phi+\beta^2]^{3/2}}$$
$$- \sum_{n=1}^{N} B_n(t)\mathscr{R}^{n-1}P_n'(\cos\phi)\sin\phi, \tag{2.12}$$

and similar expressions apply for the two velocity components U_2 and W_2 at the interface, in outer fluid 2.

Now the first kinematic boundary condition, (2.5) with $j=1$, is Fourier analysed using the orthogonality conditions for Legendre polynomials (these are given in Forbes (2011*b*) and Forbes (2014*a*) for spherical coordinates). This immediately yields the ordinary differential equations

$$H_0'(t) = -A'(t) + \frac{1}{2}\int_0^{\pi}\left[U_1 - \frac{W_1}{\mathscr{R}}\frac{\partial\mathscr{R}}{\partial\phi}\right]\sin\phi\,\mathrm{d}\phi \tag{2.13}$$

and

$$H_\ell'(t) = \frac{(2\ell+1)}{2}\int_0^{\pi}\left[U_1 - \frac{W_1}{\mathscr{R}}\frac{\partial\mathscr{R}}{\partial\phi}\right]P_\ell(\cos\phi)\sin\phi\,\mathrm{d}\phi, \quad \ell=1,\ldots,N, \tag{2.14}$$

for the coefficients in the expression (2.9) for the interface shape.

As in the method proposed by Forbes *et al.* (2007), the second kinematic condition with $j=2$ in the system (2.5) is replaced by the difference of the two, written as

$$\mathscr{R}^2(U_2-U_1) = (W_2-W_1)\mathscr{R}\frac{\partial\mathscr{R}}{\partial\phi}. \tag{2.15}$$

This equation is now subject to Fourier–Legendre decomposition. The zeroth-mode contribution is derived simply by multiplying by $\sin\phi$ and integrating, and after some algebra, is found to be satisfied identically. The contribution from the ℓth Fourier mode is then obtained by multiplying by $P_\ell(\cos\phi)\sin\phi$ and integrating. Integration by parts is used, along with the second-order differential equation satisfied by the Legendre polynomials (see Kreyszig 2011, p. 175), and leads to the elegant algebraic relations

$$\sum_{n=1}^{N} S_{\ell n}^{(1)}B_n(t) + \sum_{n=1}^{N} S_{\ell n}^{(2)}C_n(t) = 0, \quad \ell=1,\ldots,N, \tag{2.16}$$

between the two sets of Fourier coefficients $B_n(t)$ and $C_n(t)$ in the expressions (2.7), (2.8). In (2.16), the two sets of intermediate functions are

$$\left.\begin{aligned} S_{\ell n}^{(1)}(t) &= \frac{1}{(n+1)}\int_0^{\pi}\mathscr{R}^{n+1}(\phi,t)P_n'(\cos\phi)P_\ell'(\cos\phi)\sin^3\phi\,\mathrm{d}\phi,\\ S_{\ell n}^{(2)}(t) &= \frac{1}{n}\int_0^{\pi}\mathscr{R}^{-n}(\phi,t)P_n'(\cos\phi)P_\ell'(\cos\phi)\sin^3\phi\,\mathrm{d}\phi. \end{aligned}\right\} \tag{2.17}$$

https://doi.org/10.1017/jfm.2016.9 Published online by Cambridge University Press

Forbes *et al.* (2007) observed that, in spite of its elegance, an equation like (2.16) presents some difficulties, since it is a purely algebraic system. Differential equations, such as those in (2.13), (2.14), would be more easily accommodated within a numerical scheme, and can be derived from (2.16) directly, by differentiation. After some algebra, the desired differential relations are obtained in the final form

$$\sum_{n=1}^{N} S^{(1)}_{\ell n} B'_n(t) + \sum_{n=1}^{N} S^{(2)}_{\ell n} C'_n(t) = -Q_\ell(t), \quad \ell = 1, \ldots, N, \tag{2.18}$$

where the intermediate quantities

$$Q_\ell(t) = \int_0^\pi [W_2 - W_1] \left[\mathscr{R} U_1 - \frac{\partial \mathscr{R}}{\partial \phi} W_1 \right] P'_\ell(\cos\phi) \sin^2\phi \, \mathrm{d}\phi \tag{2.19}$$

have been defined for convenience.

It remains to satisfy the dynamic condition (2.6). The contribution from the ℓth Fourier mode is again obtained by multiplying by $P_\ell(\cos\phi)\sin\phi$ and integrating. The term involving the arbitrary function $f(t)$ vanishes under this process, which leads to the further system of differential equations

$$D \sum_{n=1}^{N} K^{(2)}_{\ell n} C'_n(t) - \sum_{n=1}^{N} K^{(1)}_{\ell n} B'_n(t) = \frac{1}{2} J^{(1)}_\ell - \frac{1}{2} D J^{(2)}_\ell + \frac{(D-1)}{F_1^2} Y_\ell, \tag{2.20}$$

in which it is convenient to define the intermediate functions

$$\left.\begin{aligned} K^{(1)}_{\ell n}(t) &= \int_0^\pi \mathscr{R}^n P_\ell(\cos\phi) P_n(\cos\phi) \sin\phi \, \mathrm{d}\phi, \\ K^{(2)}_{\ell n}(t) &= \int_0^\pi \mathscr{R}^{-n-1} P_\ell(\cos\phi) P_n(\cos\phi) \sin\phi \, \mathrm{d}\phi, \\ J^{(1)}_\ell(t) &= \int_0^\pi (U_1^2 + W_1^2) P_\ell(\cos\phi) \sin\phi \, \mathrm{d}\phi, \\ J^{(2)}_\ell(t) &= \int_0^\pi (U_2^2 + W_2^2) P_\ell(\cos\phi) \sin\phi \, \mathrm{d}\phi, \end{aligned}\right\} \tag{2.21}$$

and

$$\begin{aligned} Y_\ell(t) \;=\; & \int_0^\pi \left[\frac{1}{\sqrt{\mathscr{R}^2 - 2\beta\mathscr{R}\cos\phi + \beta^2}} + \frac{\gamma}{\sqrt{\mathscr{R}^2 + 2\beta\mathscr{R}\cos\phi + \beta^2}} \right] \\ & \times P_\ell(\cos\phi) \sin\phi \, \mathrm{d}\phi. \end{aligned} \tag{2.22}$$

The sets of Fourier coefficients needed to construct the nonlinear time-dependent inviscid solution are now able to be calculated from these differential equations. The initial conditions are assumed simply to be that the interface starts as a sphere of dimensionless radius 1, with outflow from the two sources as given in (2.3) and (2.4). This gives the simple initial conditions $H_0(0) = 0$, $H_n(0) = 0$, $B_n(0) = C_n(0) = 0$, $n = 1, \ldots, N$. Equations (2.13) and (2.14) now immediately give the derivatives H'_0 and H'_n while (2.18) and (2.20) must be solved together as a matrix system, at each time

https://doi.org/10.1017/jfm.2016.9 Published online by Cambridge University Press

step, to provide the derivatives B_n' and C_n'. This now results in a system of $3N+1$ ordinary differential equations, that are integrated forward in time using the MATLAB routine `ode45`, which is an accurate fourth/fifth order Runge–Kutta–Fehlberg solver, with adaptive time steps. The intermediate quantities (2.17), (2.19), (2.21) and (2.22) all involve quadratures, which have been evaluated to very high precision using the Gauss–Legendre routine `lgwt` written by von Winckel (2004).

3. Linearized inviscid solution

In order to carry out a linearized approximation to the outflow from the binary source system, it is necessary to assume that the two source strengths are small and the gravitational attraction effects are also small. To this end, we now set

$$\eta_1 = \epsilon H_1; \quad \eta_2 = \epsilon H_2; \quad \frac{1}{F_1^2} = \epsilon S_1 \tag{3.1a–c}$$

for some small parameter ϵ. The two velocity potentials and the interface shape are now expressed as regular perturbation expansions in powers of ϵ, in the forms

$$\Phi_1(r, z, t) = \epsilon \hat{P}_1(r, z, t) + O(\epsilon^2), \tag{3.2a}$$
$$\Phi_2(r, z, t) = \epsilon \hat{P}_2(r, z, t) + O(\epsilon^2), \tag{3.2b}$$
$$\mathscr{R}(z, t) = 1 + \epsilon \hat{R}_1(r, z, t) + O(\epsilon^2). \tag{3.2c}$$

Equation (3.2*c*) thus indicates that the small parameter ϵ can be regarded as giving a measure of the extent of the deformation of the interface from its initial spherical shape. Now the two kinematic conditions (2.5) give rise to the linearized expressions

$$\frac{\partial \hat{P}_1}{\partial r} = \frac{\partial \hat{R}_1}{\partial t}; \quad \frac{\partial \hat{P}_2}{\partial r} = \frac{\partial \hat{R}_1}{\partial t} \quad \text{on } r = 1, \tag{3.3a,b}$$

and the dynamic condition (2.6) linearizes to

$$D\frac{\partial \hat{P}_2}{\partial t} - \frac{\partial \hat{P}_1}{\partial t} = S_1(D-1)\left[\frac{1}{\sqrt{1-2\beta\cos\phi+\beta^2}} + \frac{\gamma}{\sqrt{1+2\beta\cos\phi+\beta^2}}\right] \quad \text{on } r = 1. \tag{3.4}$$

The expansion (3.2) and the approximate interface conditions (3.3), (3.4) show that this linearized problem will be equivalent, in some sense, to a small-time solution, since the interface is assumed not to deviate greatly from its initial spherical configuration $r = 1$.

Since the linearized velocity potentials must still satisfy Laplace's equation and conditions (2.3), (2.4) at the two sources, it is appropriate to assume

$$\hat{P}_1(r, \phi, t) = -\frac{H_1}{4\pi\sqrt{r^2-2\beta r\cos\phi+\beta^2}} - \frac{H_2}{4\pi\sqrt{r^2+2\beta r\cos\phi+\beta^2}} + \sum_{n=1}^{\infty} \hat{B}_n(t) r^n P_n(\cos\phi), \quad r < 1, \tag{3.5}$$

https://doi.org/10.1017/jfm.2016.9 Published online by Cambridge University Press

and

$$\hat{P}_2(r,\phi,t) = -\frac{H_1}{4\pi\sqrt{r^2-2\beta r\cos\phi+\beta^2}} - \frac{H_2}{4\pi\sqrt{r^2+2\beta r\cos\phi+\beta^2}} + \sum_{n=1}^{\infty}\hat{C}_n(t)r^{-n-1}P_n(\cos\phi), \quad r>1, \tag{3.6}$$

as for the nonlinear forms (2.7), (2.8). The linearized kinematic conditions (3.3) lead at once to the conclusion

$$n\hat{B}_n(t) = -(n+1)\hat{C}_n(t). \tag{3.7}$$

The two forms (3.5) and (3.6) for the linearized velocity potentials and the relation (3.7) are now used in the linearized dynamic condition (3.4). The resulting equation is Fourier analysed, by multiplying by $P_\ell(\cos\phi)\sin\phi$ and integrating, to give the contribution from the ℓth mode. This gives

$$\left[D+\frac{\ell+1}{\ell}\right]\hat{C}'_\ell(t)\frac{2}{2\ell+1} = S_1(D-1)\left[\int_0^\pi \frac{P_\ell(\cos\phi)\sin\phi\,\mathrm{d}\phi}{\sqrt{1-2\beta\cos\phi+\beta^2}} + \int_0^\pi \frac{\gamma P_\ell(\cos\phi)\sin\phi\,\mathrm{d}\phi}{\sqrt{1+2\beta\cos\phi+\beta^2}}\right], \quad \ell=1,\ldots,N. \tag{3.8}$$

The two integrals in this expression can be evaluated in closed form, using the generating functions for the Legendre polynomials (see Gradshteyn & Ryzhik 2000, p. 978) leading to

$$\int_0^\pi \frac{P_\ell(\cos\phi)\sin\phi\,\mathrm{d}\phi}{\sqrt{1-2\beta\cos\phi+\beta^2}} = \beta^\ell\frac{2}{2\ell+1}. \tag{3.9}$$

Equation (3.8) is now easily integrated with respect to time, and it follows from (3.7) that

$$\left.\begin{aligned}\hat{B}_n(t) &= -tS_1(D-1)\frac{(n+1)\beta^n[1+\gamma(-1)^n]}{Dn+(n+1)},\\ \hat{C}_n(t) &= tS_1(D-1)\frac{n\beta^n[1+\gamma(-1)^n]}{Dn+(n+1)}.\end{aligned}\right\} \tag{3.10}$$

When combined with the series forms (3.5), (3.6), these relations (3.10) give the complete forms for the two velocity potentials.

The interface shape is now available from (3.3), after a further integration with respect to time. Using the relations (3.1) to recover the original dimensionless parameters gives the linearized shape in the final form

$$\mathscr{R}(\phi,t) = 1+\frac{t}{4\pi}\left[\frac{\eta_1(1-\beta\cos\phi)}{[1-2\beta\cos\phi+\beta^2]^{3/2}} + \frac{\eta_2(1+\beta\cos\phi)}{[1+2\beta\cos\phi+\beta^2]^{3/2}}\right] - \frac{t^2(D-1)}{2F_1^2}\sum_{n=1}^{\infty}\frac{n(n+1)\beta^n[1+\gamma(-1)^n]}{Dn+(n+1)}P_n(\cos\phi)+O(\epsilon^2). \tag{3.11}$$

This expression (3.11) is evaluated numerically to good accuracy, typically by summing the first fifty or so terms in the series. Convergence is good, since $\beta<1$.

https://doi.org/10.1017/jfm.2016.9 Published online by Cambridge University Press

Forbes (2011*b*) observed that outflow from a single source was most likely to occur as a one-sided jet, since that is the most unstable mode, and therefore the one that grows most rapidly and dominates all the others. Consequently, Forbes (2014*a*) was keen to explore situations that might lead to a more bipolar outflow shape, as is often observed in astrophysics. It is therefore appropriate to ask the same question of the linearized solution (3.11) in the present outflow geometry, with two point sources present. Mathematically, true bipolar symmetry requires $\mathscr{R}(\phi, t) = \mathscr{R}(\pi - \phi, t)$, and a necessary condition for this to occur is that the two source strengths should be equal; $\eta_1 = \eta_2$. In addition, since $P_n(\cos(\pi - \phi)) = P_n(-\cos\phi)$, then it follows that bipolar symmetry will be possible only when the even-order Legendre polynomials alone are involved, since these possess just the even powers of their arguments. From (3.11), the odd-mode Legendre polynomials in the sum term cancel precisely when $\gamma = 1$ only. Therefore, according to linearized theory, the outflow from the two-source system can only be symmetrically bipolar if the sources have equal strength, $\eta_1 = \eta_2$, and the two masses are equal, $\gamma = 1$, and therefore have equal gravitational attraction. This accords with physical intuition.

4. Viscous fluid model

It is desirable also to understand the role of viscosity in the formation of these outflows, and that is done here using a Boussinesq formulation to simplify the problem. Such an approach was used by Forbes (2011*b*, 2014*a*) for the case of a single point source in axisymmetric three-dimensional flow, and has been generalized more recently by Forbes (2014*b*) to account for the presence of two line sources in planar two-dimensional flow. Here, the technique must be developed further to model the presence of two point sinks in axisymmetric outflow in three dimensions. Dimensionless variables are again used, as in § 2.

In the Boussinesq approximation, the fluid density ρ is supposed to consist of its contribution $\rho = 1$ from the inner fluid and the two point sources, and a small perturbation component $\bar{\rho}$. Thus $\rho = 1 + \bar{\rho}$ and necessarily $\bar{\rho} = 0$ in the inner fluid 1, and $\bar{\rho} = (D - 1)$ in surrounding fluid 2. Since the density perturbation is small, $(D - 1)$ must also be small. The Boussinesq approximation thus convects the density perturbation $\bar{\rho}$ around with the moving fluid, and as discussed in Forbes (2014*a*), this variable may alternatively be thought of as temperature, or perhaps even as a marker for salinity.

Crucially, the Boussinesq approximation ignores the presence of a mathematical interface of infinitesimal thickness between the two fluids, replacing it instead with an interfacial mixing zone of narrow, but finite, width. In its simplest form, Boussinesq theory thus considers the two-fluid system as just a single fluid of continuously-varying density, in which there is an interfacial zone, necessarily of finite thickness, across which the density varies rapidly but smoothly from its true value in the inner fluid to its corresponding value in the outer medium. This is done originally to simplify the algebra in the formulation of the problem, since the exact viscous conditions at the interface (see Batchelor 1967, p. 150) can simply be ignored. Moore (1979) proved that, for inviscid fluids, the interface between them develops a curvature singularity within finite time, and Forbes (2009) demonstrated numerically that this inviscid singularity is replaced by a small but finite region of very high vorticity in the viscous case, and this causes the interface to roll up as time progresses. However, it has been shown very recently by Forbes *et al.* (2015) that, even in the viscous case, a mathematical thin interface may still form curvature

https://doi.org/10.1017/jfm.2016.9 Published online by Cambridge University Press

singularities within finite time, although by a different mechanism to the Moore (1979) curvature singularity at the interface between inviscid fluids. This surprising result was demonstrated asymptotically as well as numerically. So another major advantage of the Boussinesq approximation is that it happens to avoid all these difficulties, by dealing instead with a finite-width interfacial zone instead of a precise mathematical discontinuity.

In the Boussinesq approximation, the Navier–Stokes equations of viscous flow become

$$\frac{\partial \boldsymbol{q}}{\partial t} + (\boldsymbol{q}\cdot\boldsymbol{\nabla})\boldsymbol{q} + \boldsymbol{\nabla} p = -\frac{1}{F_1^2}(1+\bar{\rho})\boldsymbol{f} + \frac{1}{R_e}\nabla^2\boldsymbol{q}. \tag{4.1}$$

Here, the constant $R_e = (\rho_1 m_R)/(\mu a)$ is a Reynolds number based on the dimensional initial radius a of the sphere, the dynamic viscosity μ and the (unspecified) reference volume flow rate m_R as in § 2. The Froude number is again F_1 and $\boldsymbol{f}$ is the combined gravitational force per mass of the two sources. As in the work of Forbes (2011*b*), it is again convenient here to work with the vorticity $\boldsymbol{\zeta} = \operatorname{curl}\boldsymbol{q} = \zeta_\theta \boldsymbol{e}_\theta$ which only has the one component in the azimuthal θ-direction, for axisymmetric flow. In spherical polar coordinates, this vorticity component is given in terms of the velocity components as

$$\zeta_\theta = \frac{1}{r}\left[\frac{\partial}{\partial r}(rw) - \frac{\partial u}{\partial \phi}\right]. \tag{4.2}$$

A vorticity equation is now derived by taking the vector curl of the Boussinesq Navier–Stokes equation (4.1). After some considerable algebra, the result is found to be

$$\begin{aligned}
&\frac{\partial \zeta_\theta}{\partial t} + u\frac{\partial \zeta_\theta}{\partial r} + \frac{w}{r}\frac{\partial \zeta_\theta}{\partial \phi} - \frac{\zeta_\theta}{r}[u + w\cot\phi] \\
&\quad = \frac{1}{F_1^2[r^2 - 2\beta r\cos\phi + \beta^2]^{3/2}}\left[\frac{(r-\beta\cos\phi)}{r}\frac{\partial \bar{\rho}}{\partial \phi} - \beta\sin\phi\frac{\partial \bar{\rho}}{\partial r}\right] \\
&\qquad + \frac{\gamma}{F_1^2[r^2 + 2\beta r\cos\phi + \beta^2]^{3/2}}\left[\frac{(r+\beta\cos\phi)}{r}\frac{\partial \bar{\rho}}{\partial \phi} + \beta\sin\phi\frac{\partial \bar{\rho}}{\partial r}\right] \\
&\qquad + \frac{1}{R_e}\left[\frac{1}{r^2}\frac{\partial}{\partial r}\left(r^2\frac{\partial \zeta_\theta}{\partial r}\right) + \frac{1}{r^2\sin\phi}\frac{\partial}{\partial \phi}\left(\sin\phi\frac{\partial \zeta_\theta}{\partial \phi}\right) - \frac{\zeta_\theta}{r^2\sin^2\phi}\right].
\end{aligned} \tag{4.3}$$

Many of the terms in this equation may be checked against the similar expressions given in Batchelor (1967, p. 601).

In the Boussinesq approximation, the mass conservation equation is 'split' into an essentially incompressible part and a transport equation for the density perturbation $\bar{\rho}$, to give the two equations

$$\left.\begin{aligned}
\operatorname{div}\boldsymbol{q} &= 0, \\
\frac{\partial \bar{\rho}}{\partial t} + \boldsymbol{q}\cdot\boldsymbol{\nabla}\bar{\rho} &= \sigma\nabla^2\bar{\rho}.
\end{aligned}\right\} \tag{4.4}$$

The first of the conditions in the system (4.4) is satisfied identically by making use of a streamfunction $\Psi(r, \phi, t)$, in terms of which the two velocity components may be written

$$u = \frac{1}{r\sin\phi}\frac{\partial}{\partial \phi}(\Psi\sin\phi); \quad w = -\frac{1}{r}\frac{\partial}{\partial r}(r\Psi). \tag{4.5a,b}$$

https://doi.org/10.1017/jfm.2016.9 Published online by Cambridge University Press

The two functions to be found in this formulation are therefore the density perturbation $\bar{\rho}$ and the streamfunction Ψ, and they are the solutions to the vorticity equation (4.3) and the transport equation in the system (4.4).

A spectral representation for these two functions is now sought. An artificial 'computational boundary' is introduced at some spherical surface $r = R$, and the aim is then to create a representation for the streamfunction Ψ that gives a similar form for the vorticity component ζ_θ. After some algebra, the appropriate form is found to be

$$\Psi(r,\phi,t) = \frac{\eta_1(\beta - r\cos\phi)}{4\pi r\sin\phi\sqrt{r^2-2r\beta\cos\phi+\beta^2}} - \frac{\eta_2(\beta + r\cos\phi)}{4\pi r\sin\phi\sqrt{r^2+2r\beta\cos\phi+\beta^2}} + \sum_{m=1}^{M}\sum_{n=1}^{N} A_{mn}(t)\frac{1}{\sqrt{r}}\mathrm{J}_{n+1/2}(\alpha_{nm}r)P_n'(\cos\phi)\sin\phi. \tag{4.6}$$

In this expression, the function $\mathrm{J}_{n+1/2}$ is the first-kind Bessel function of order $n+1/2$ and is related to the spherical Bessel functions (see Abramowitz & Stegun 1972, p. 360). The function P_n is the Legendre polynomial of degree n (Gradshteyn & Ryzhik 2000, § 8.91) and P_n' is its derivative. Expressions similar to (4.6) were used by Forbes (2011*b*, 2014*a*). The additional constants appearing in this representation are defined to be

$$\alpha_{nm} = j_{n+1/2,m}/R, \tag{4.7}$$

in which the symbol $j_{n+1/2,m}$ denotes the mth zero of the Bessel function $\mathrm{J}_{n+1/2}$. These have been calculated here using the simple bisection method and asymptotic estimates for these zeros given in Abramowitz & Stegun (1972, p. 371). The task is to calculate the time-dependent Fourier coefficients $A_{mn}(t)$ in this representation (4.6).

It follows from (4.5) that the two velocity components now become

$$u(r,\phi,t) = \frac{\eta_1(r-\beta\cos\phi)}{4\pi[r^2-2r\beta\cos\phi+\beta^2]^{3/2}} + \frac{\eta_2(r+\beta\cos\phi)}{4\pi[r^2+2r\beta\cos\phi+\beta^2]^{3/2}} + \sum_{m=1}^{M}\sum_{n=1}^{N} n(n+1)A_{mn}(t)\frac{1}{r^{3/2}}\mathrm{J}_{n+1/2}(\alpha_{nm}r)P_n(\cos\phi) \tag{4.8}$$

and

$$w(r,\phi,t) = \frac{\eta_1\beta\sin\phi}{4\pi[r^2-2r\beta\cos\phi+\beta^2]^{3/2}} - \frac{\eta_2\beta\sin\phi}{4\pi[r^2+2r\beta\cos\phi+\beta^2]^{3/2}} - \sum_{m=1}^{M}\sum_{n=1}^{N} A_{mn}(t)\left[\frac{1}{2r^{3/2}}\mathrm{J}_{n+1/2}(\alpha_{nm}r) + \frac{\alpha_{nm}}{\sqrt{r}}\mathrm{J}_{n+1/2}'(\alpha_{nm}r)\right]P_n'(\cos\phi)\sin\phi. \tag{4.9}$$

These two velocity components with (4.2) give

$$\zeta_\theta(r,\phi,t) = \sum_{m=1}^{M}\sum_{n=1}^{N} A_{mn}(t)\frac{\alpha_{nm}^2}{\sqrt{r}}\mathrm{J}_{n+1/2}(\alpha_{nm}r)P_n'(\cos\phi)\sin\phi \tag{4.10}$$

as the final form for the representation of the vorticity component.

A spectral representation is also needed for the density perturbation function $\bar{\rho}$. The selection of an appropriate form turns out to be a difficult problem, and all the more

https://doi.org/10.1017/jfm.2016.9 Published online by Cambridge University Press

so in this case because of the two point sources located within inner fluid 1. For the case of planar flow with two line sources, Forbes (2014*b*) coped with this difficulty by multiplying the governing equations by functions that vanished at the locations of the two line sources; this is adequate for solving the problem, but possibly may not give an entirely faithful representation of the density perturbation function at the sources themselves. Accordingly, it seemed preferable here to use a form

$$\bar{\rho}(r,\phi,t) = (D-1)\mathscr{H}(r,\phi) \times \left[1 + \sum_{m=1}^{M} C_{m0}(t)\cos(\alpha_{0m}r) + \sum_{m=1}^{M}\sum_{n=1}^{N} C_{mn}(t)\frac{1}{\sqrt{r}}\mathrm{J}_{n+1/2}(\alpha_{nm}r)P_n(\cos\phi)\right], \quad (4.11)$$

since this representation can satisfy exactly the condition that $\bar{\rho} = 0$ at the locations of the two point sources in this problem. Here, additional constants

$$\alpha_{0m} = (2m-1)\pi/(2R) \quad (4.12)$$

have been defined for convenience. It is necessary to choose the function $\mathscr{H}(r,\phi)$ in (4.11) carefully, both to satisfy the requirements that the density perturbation should be zero at the two source points as well as to become 1 at large radius r, so as to avoid numerical ill conditioning and give the correct value $\bar{\rho} \to (D-1)$ far away. An appropriate choice is therefore

$$\mathscr{H}(r,\phi) = \frac{[r^2 - 2\beta r\cos\phi + \beta^2][r^2 + 2\beta r\cos\phi + \beta^2]}{[r^2+\beta^2]^2}. \quad (4.13)$$

It now turns out that, with this choice (4.13) for the function $\mathscr{H}$ in the representation (4.11) for the density perturbation function, no further manipulation of the governing equations is needed in the spectral solution method. However, the presence of the function $\mathscr{H}$ in (4.11) effectively means that the basis functions in the spectral solution for $\bar{\rho}$ are no longer orthogonal.

The representation (4.10) is substituted into the vorticity equation (4.3), and the resulting expression is Fourier decomposed, by multiplying by

$$r^{3/2}\mathrm{J}_{\ell+1/2}(\alpha_{\ell k}r)P'_{\ell}(\cos\phi)\sin^2\phi \quad (4.14)$$

and integrating over the domain $0 < r < R$, $0 < \phi < \pi$. The derivatives P'_n of the Legendre polynomials obey an orthogonality condition, which is given by Forbes (2011*b*) in these spherical coordinates. The Bessel functions $\mathrm{J}_{n+1/2}$ are also orthogonal with respect to the weight function r and so a set of ordinary differential equations is obtained, for the unknown coefficients $A_{mn}(t)$. For completeness, these are given in the appendix A.

The expression (4.11) is similarly substituted into the transport equation for $\bar{\rho}$, the second in the system (4.4). The resulting equation is lengthy, primarily due to the Laplacian term $\sigma\nabla^2\bar{\rho}$ on the right-hand side and the presence of the additional function $\mathscr{H}$ in (4.11). A zeroth Fourier-mode contribution in ϕ is first derived by multiplying by $\cos(\alpha_{0k}r)\sin\phi$ and integrating. This gives a set of M differential equations of the general form

$$\sum_{m=1}^{M}\mathscr{M}_{m0k0}C'_{m0}(t) + \sum_{m=1}^{M}\sum_{n=1}^{N}\mathscr{N}_{mnk0}C'_{mn}(t) = R_{k0}, \quad k = 1,\ldots,M, \quad (4.15)$$

https://doi.org/10.1017/jfm.2016.9 Published online by Cambridge University Press

in which the constants $\mathscr{M}_{m0k0}$ and so on are presented in the appendix A. Higher Fourier-mode contributions are similarly obtained by multiplying the density transport equation in (4.4) by

$$r^{3/2}\mathrm{J}_{\ell+1/2}(\alpha_{\ell k}r)P_\ell(\cos\phi)\sin\phi \tag{4.16}$$

and integrating, as before. This results in a further set of differential equations with the general forms

$$\sum_{m=1}^{M}\mathscr{M}_{m0k\ell}C'_{m0}(t)+\sum_{m=1}^{M}\sum_{n=1}^{N}\mathscr{N}_{mnk\ell}C'_{mn}(t)=R_{k\ell},\quad k=1,\ldots,M,\,\ell=1,\ldots,N, \tag{4.17}$$

in which the constants $\mathscr{M}_{m0k\ell}$ and so on are again given in the appendix A.

This system of $M(N+1)$ differential equations (4.15), (4.17) is set up as an $M(N+1)\times M(N+1)$ linear matrix equation for a vector containing all the derivatives $C'_{m0}(t)$, $C'_{mn}(t)$ and must first be solved for these derivatives at each new time step. In fact, the coefficient matrix is independent of time t, and so only needs to be inverted once, and its inverse cached in memory at the beginning of the algorithm. In this way, although the basis functions for the representation of $\bar{\rho}$ in (4.11) are no longer orthogonal, in practice this does not incur too great an additional numerical cost.

Now the system of $M(2N+1)$ differential equations (A 1), (4.15) and (4.17) is integrated forward in time, using the MATLAB routine `ode45`, as in § 2. There are many quantities in these expressions involving terms defined in terms of integrals, as is evident from (A 1), (A 6) and (A 7) in the appendix A. These quadratures are all evaluated numerically, using the Gaussian routine `lgwt` written by von Winckel (2004). It has been found that making use of 121 mesh points in r and the same number in ϕ enables these quadratures to be performed to very high accuracy. Results are typically obtained with $M=N=31$ coefficients, and as demonstrated by Forbes (2014*a*), this gives sufficient accuracy to resolve the features of interest in these evolving outflows.

The initial condition is chosen to mimic that used for the inviscid solution in §§ 2 and 3. The initial velocity is just that due to the presence of the two sources, and thus the coefficients in the series for streamfunction are set initially to zero, so that

$$A_{k\ell}(0)=0,\quad k=1,\ldots,M,\,\ell=1,\ldots,N. \tag{4.18}$$

The density perturbation function is initially zero inside the unit sphere and $(D-1)$ outside it, so that the condition

$$\bar{\rho}(r,\phi,0)=\begin{cases}0 & \text{if } r<1,\\ (D-1) & \text{if } r>1,\end{cases} \tag{4.19}$$

must be satisfied. In order to impose this initial condition (4.19), the representation (4.11) must be subject to Fourier decomposition, as previously. This leads to the system of algebraic equations

$$\sum_{m=1}^{M}\mathscr{M}_{m0k0}C_{m0}(0)+\sum_{m=1}^{M}\sum_{n=1}^{N}\mathscr{N}_{mnk0}C_{mn}(0)=\int_0^R\int_0^\pi\left[\frac{\bar{\rho}(r,\phi,0)}{(D-1)}-\mathscr{H}\right]\times\cos(\alpha_{0k}r)\sin\phi\,\mathrm{d}\phi\,\mathrm{d}r,\quad k=1,\ldots,M, \tag{4.20}$$

https://doi.org/10.1017/jfm.2016.9 Published online by Cambridge University Press

and

$$\sum_{m=1}^{M} \mathscr{M}_{m0k\ell} C_{m0}(0) + \sum_{m=1}^{M}\sum_{n=1}^{N} \mathscr{N}_{mnk\ell} C_{mn}(0) = \int_0^R \int_0^\pi \left[\frac{\bar{\rho}(r,\phi,0)}{(D-1)} - \mathscr{H} \right] \times r^{3/2} \mathrm{J}_{\ell+1/2}(\alpha_{\ell k} r) P_\ell(\cos\phi) \sin\phi \, \mathrm{d}\phi \, \mathrm{d}r, \quad k = 1, \ldots, M, \ell = 1, \ldots, N. \tag{4.21}$$

These expressions involve further quadratures, which are again evaluated using the Gaussian routine `lgwt` written by von Winckel (2004). However, the left-hand sides of these two equations (4.20), (4.21) have the same algebraic structure as the differential equations (4.15), (4.17), and involve precisely the same sets of constants. Accordingly, the inverse of the large $M(N+1) \times M(N+1)$ matrix already calculated and stored at the beginning of the algorithm can again be used to solve this linear matrix equation system (4.20), (4.21) for the initial values of the coefficients $C_{m0}(0)$, $C_{mn}(0)$ in the representation of the density perturbation.

5. Discussion of results

The algorithms for generating nonlinear solutions to the inviscid and viscous models, discussed in §§ 2 and 4, have been tested extensively across a wide range of parameter values, to assess the behaviour of the solution at different values and to confirm convergence of the results at different numbers of Fourier coefficients. Due to the spherical nature of the interface, it turns out that there is no particular difference in the results for $D < 1$ and $D > 1$. This is because, in this geometry, it is not just the Rayleigh–Taylor instability influencing the outcome, but also the Bell–Plesset instability due to the curvature of the interface itself (see Epstein 2004). In order to simplify the presentation of results, therefore, only a density ratio $D = 1.05$ will be considered here, in which the surrounding fluid is 5 % heavier than inner fluid 1. Similarly, the role of the Froude number F_1 in the results is largely to affect the time scale over which features evolve, and so just the single value $F_1 = 10$ will be discussed.

Figure 2 gives a comparison of inviscid results, for the nonlinear algorithm discussed in § 2 and the linearized solution of § 3. The nonlinear solutions are drawn with heavy solid lines and the linearized results are indicated with lighter dashed lines. At the early time $t = 2$ there is almost complete agreement between the two theories, as is evident in the figure. However the linearized theory, which is predicated on the assumption that the interface remains close to the initial sphere $r = 1$, progressively overestimates the extent of the outflow, and particularly near the poles of the original sphere, close to the z-axis. In this sense, the linearized theory can be thought of as an early-time approximation in this instance, as suggested in § 3. Nevertheless, there is still reasonable agreement over most of the interface away from the two polar regions, and this is evident in the profiles at the intermediate time $t = 10$.

From the mathematical point of view, it is possible to consider the situation in which one of the sources within the jacket of the inner fluid region has negative strength, and so becomes a point sink, even if the relevance of such a calculation to astrophysics is questionable. For interest, such a situation is illustrated in figure 3. In these pictures, the solution is shown for $\eta_1 = 0.1$, $\eta_2 = -0.1$ so that the top singularity is a source that ejects fluid, but the bottom one is a sink that removes fluid at the

https://doi.org/10.1017/jfm.2016.9 Published online by Cambridge University Press

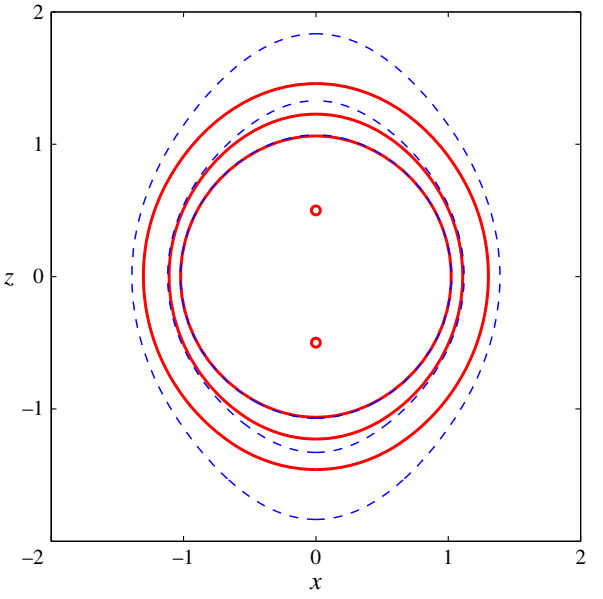


FIGURE 2. (Colour online) A comparison of the growth of the interface in the inviscid model, for the linearized (dashed; blue online) and nonlinear (heavy solid line; red online) theories. Solutions are shown at the three different times $t = 2$, 10 and 30. The source location parameter is $\beta = 0.5$ and their strengths are $\eta_1 = \eta_2 = 0.1$. The two masses are equal, so $\gamma = 1$. The two small circles (red online) give the source locations.

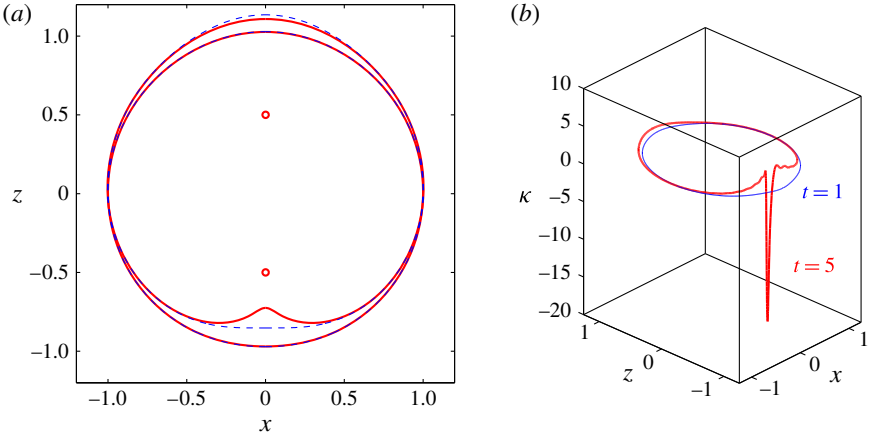


FIGURE 3. (Colour online) Evolution of the interface in the inviscid model at two different times $t = 1$ and 5. The source location parameter is $\beta = 0.5$ and the upper source has strength $\eta_1 = 0.1$ while the strength of the lower sink is $\eta_2 = -0.1$. The two masses are equal, so $\gamma = 1$. (*a*) Interface location for the linearized (dashed; blue online) and nonlinear (heavy solid line; red online) theories. The two small circles (red online) give the source locations. (*b*) Interfacial curvatures.

same volume rate. Overall, there is no nett production of fluid so that, on average, the interface location would be expected to remain as $r = 1$. Again the masses are equal so that $\gamma = 1$ and the location of the two singularities is $\beta = 0.5$.

https://doi.org/10.1017/jfm.2016.9 Published online by Cambridge University Press

Figure 3(*a*) illustrates the two interface profiles at the two times $t = 1$ and $t = 5$, for both the linearized and nonlinear theories. The linearized predictions are drawn with dashed lines and the nonlinear results are indicated by thicker solid lines. The two theories are essentially indistinguishable at time $t = 1$. However, at the later time $t = 5$, the linearized theory again overpredicts the outflow near the upper source, and particularly so in the vicinity of the pole of the initial sphere on the upper portion of the z-axis. By contrast, near the lower point, which is a sink, the linearized theory underestimates the extent to which the interface in the inviscid theory is pulled upwards on the diagram, towards the lower sink.

The sudden withdrawal of the interface toward the sink is a phenomenon dominated by nonlinear effects, as was originally demonstrated by Tuck & Vanden-Broeck (1984) and more recently in unsteady selective withdrawal flows by Stokes *et al.* (2003), for example. Forbes & Hocking (2007) showed that withdrawal into a drain is ultimately limited by the apparent formation of curvature singularities at the interface, in inviscid flow, similar in many respects to the Moore curvature singularity (Moore 1979). This appears to be true in the present situation, too. Figure 3(*b*) shows the interfacial curvatures κ for the two solutions in figure 3(*a*), at the two times $t = 1$ and $t = 5$. These have been calculated from the formula

$$\kappa = \frac{\mathscr{R}^2 + 2\mathscr{R}_\phi^2 - \mathscr{R}\mathscr{R}_{\phi\phi}}{(\mathscr{R}^2 + \mathscr{R}_\phi^2)^{3/2}}, \tag{5.1}$$

which may be derived in spherical polar coordinates (2.1) from the formula for curvature given by Kreyszig (2011, p. 392). One of the advantages of the spectral technique presented in § 2 is that a difficult quantity such as the curvature in (5.1) can be calculated to very high accuracy by exact differentiation of the representation (2.9) for the nonlinear interface $r = \mathscr{R}(\phi, t)$; this was used by Forbes *et al.* (2015) to predict a curvature singularity in viscous Kelvin–Helmholtz flow, that was later confirmed analytically.

It may be seen from figure 3(*b*) that the interfacial curvature κ at the early time $t = 1$ is approximately constant, at the value $\kappa \approx 1$, consistently with the interface lying on a sphere of unit radius. However, at the later time $t = 5$, a sharp negative spike of curvature has formed directly below the sink, at the point on the lower portion of the z-axis. This spike forms rapidly as time progresses, and in fact the result shown was the last time for which the numerical method could give a solution. It therefore appears to be the case that the solution with a sink is ultimately limited by the formation of a curvature singularity within finite time, as the interface is drawn in toward the sink.

The predictions of the viscous model in § 4 are now investigated, for the same case as shown in figure 2 for the inviscid case. The result is displayed in figure 4. The two sources have equal strengths $\eta_1 = \eta_2 = 0.1$ and they are located at half the initial radius of the sphere, so that $\beta = 0.5$. Their masses are equal; $\gamma = 1$. Viscous outflows are shown at the three different times $t = 4$, $t = 10$ and $t = 13$, and consist of contour diagrams for the density perturbation function $\bar{\rho}$ at these three times. In the outer region, representing fluid 2 in figure 1, the density perturbation has the value $\bar{\rho} = 0.05$. The slightly mottled appearance of the shaded contours in this region is caused by the presence of waves of very small amplitude; these are numerical in origin, and are a consequence of Gibbs' phenomenon (see Kreyszig 2011, p. 515) associated with the discontinuity in the initial condition (4.19) and are of no significance.

https://doi.org/10.1017/jfm.2016.9 Published online by Cambridge University Press

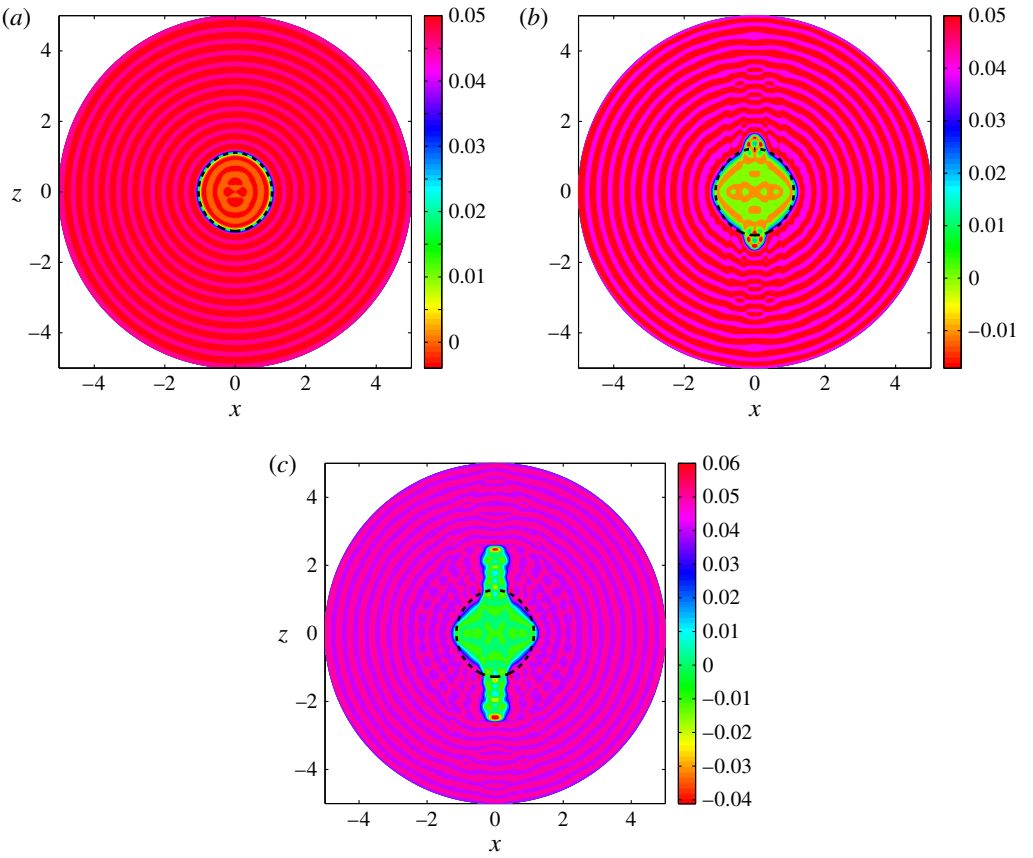


FIGURE 4. (Colour online) Evolution of the outflow in the viscous model at the three times (*a*) $t=4$, (*b*) $t=10$ and (*c*) $t=13$. The source location parameter is $\beta=0.5$ and the two sources have strengths $\eta_1=\eta_2=0.1$. The two masses are equal, so $\gamma=1$. Contours of the density perturbation $\bar{\rho}$ are shown. The heavy dashed lines are the nonlinear inviscid predictions at each time.

Also shown on the diagrams in figure 4 are the predictions of the nonlinear inviscid solution for the interface shape $r=\mathscr{R}(\phi, t)$ at the three times. These inviscid results are drawn with heavy dashed lines on each diagram. The viscous and inviscid results are clearly in very good agreement at early times. Thus the inviscid interface for time $t=4$ in figure 4(*a*) lies precisely within the narrow interfacial zone in the viscous solution, where the density function $\bar{\rho}$ changes smoothly but rapidly, as is evident from that picture. At later times, an interesting qualitative difference emerges, however, between the predictions of these two models. In the inviscid theory, the interface continues to grow in a nearly spherical shape, except for slight bulges near the two poles on the z-axis. Such behaviour was also encountered in figure 2. On the other hand, the viscous model indicates that, while growth also begins this way for earlier times, there comes a time when small nodules appear near the two poles of the sphere, and these then grow rapidly outwards. Thus, in figure 4(*b*), while there is still reasonably good agreement between the viscous and inviscid predictions as to the location and shape of the interfacial zone at time $t=10$, there are two small 'buds' that have developed in the viscous solution near the poles. These then grow

https://doi.org/10.1017/jfm.2016.9 Published online by Cambridge University Press

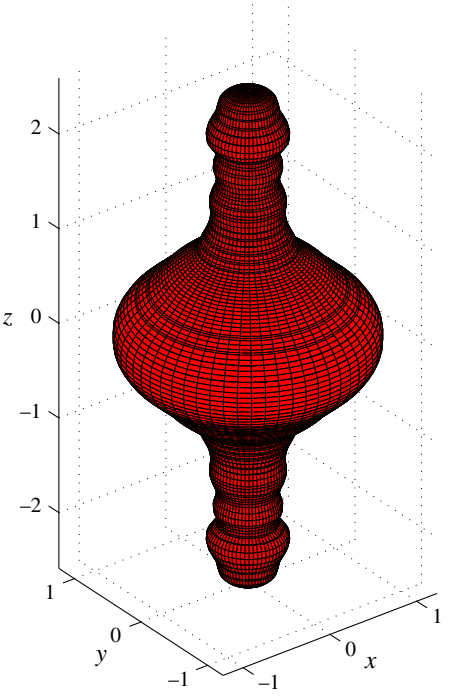


FIGURE 5. (Colour online) Perspective view of the interface for the viscous solution at time $t = 13$, for the case $\beta = 0.5$ and source strengths $\eta_1 = \eta_2 = 0.1$. The two masses are equal, so $\gamma = 1$.

rapidly, so that a short time later, they have developed into the pronounced bipolar jets in figure 4(*c*) at time $t = 13$. The rapid development of these jets is a significant challenge to numerical solution techniques, and the result for $t = 13$ is the largest time for which these viscous solutions could be computed at this value of the source location parameter β.

Figure 5 shows the effective interface for the viscous solution at time $t = 13$, displayed in figure 4(*c*). This diagram serves as a reminder that these outflows are indeed three dimensional, although axisymmetric. The interfacial surface in this picture was created by taking the contour $\bar{\rho} = 0.02$ in figure 4(*c*) and rotating it about the z-axis. The scales on all three axes are the same, so that the outflow jets are as they would actually appear. Smaller secondary waves along the jets are visible in this image, and represent a type of viscous Kelvin–Helmholtz instability, with small toroidal vortices formed in the outer fluid surrounding each jet.

It is interesting to study the evolution of the vorticity function ζ_θ in the outflow, and this is shown for the same parameters as in figures 4 and 5, at the last time $t = 13$ for which viscous solutions could be found. In a study of the Rayleigh–Taylor instability, Forbes (2009) demonstrated that the flow was essentially irrotational everywhere, except for relatively small regions near the interface, where vorticity was generated through viscous shear. Similar observations were made in relation to the one-sided outflow jets produced by a single point source (Forbes 2011*b*, 2014*a*). Figure 6 shows that a similar situation applies here, too. The vorticity is largely zero throughout the fluid, except in a narrow jacket around each outflow jet. This accounts for the very different outflow shapes between the inviscid and viscous solutions at later times.

https://doi.org/10.1017/jfm.2016.9 Published online by Cambridge University Press

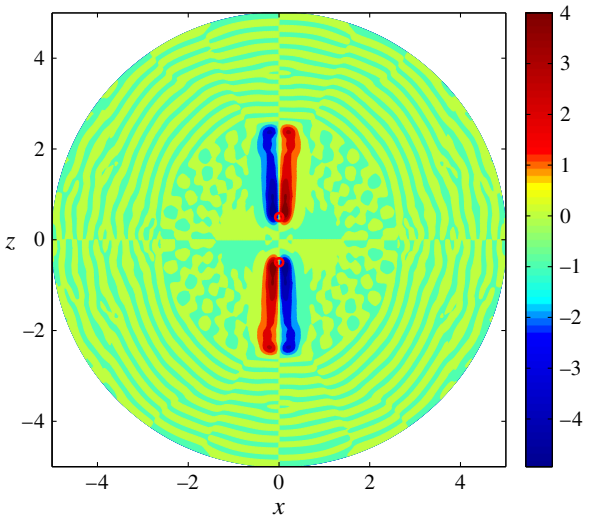


FIGURE 6. (Colour online) Contours of the vorticity for the viscous solution at time $t = 13$, for the case $\beta = 0.5$ and source strengths $\eta_1 = \eta_2 = 0.1$. The two masses are equal, so $\gamma = 1$. The two small circles (red online) give the source locations.

The development of the outflow jets may also be understood through a study of the streamsurfaces associated with the flow. Since the flow is axisymmetric, it has a streamfunction Ψ, given by the expression (4.6). It is straightforward to prove that level surfaces of the function

$$r \sin\phi \, \Psi(r, \phi, t) \tag{5.2}$$

are streamsurfaces for the flow, since tangents to these level surfaces are parallel to the fluid velocity vector.

Figure 7 illustrates the evolution of the streamlines on the plane $y = 0$, for the same flow discussed in figures 4–6, at the three times $t = 4$, 10 and 13. The function in (5.2) was created from the spectral representation (4.6) and contoured at 21 equally-spaced levels. Cartesian x and z were then created and plotted in figure 7. The scales on the axes are equal, and the locations of the two sources are indicated by small circles. At the early time $t = 4$ in figure 7(*a*), the streamline pattern is clearly dominated by the two sources; there is a plane of symmetry at $z = 0$ and each source produces the classical streamline pattern associated with a source placed next to the effective wall at this plane of symmetry. As time progresses, however, this pattern changes markedly, with the development of additional secondary vortices around the two jets. These are clearly visible in figure 7(*b*,*c*) at times $t = 10$ and 13, and are responsible to a large extent for the shape of the outflows.

The behaviour of the outflow jets is strongly affected by the locations β of the two sources. Since the sources are located within the initial sphere of unit radius, it follows that $\beta < 1$, and as β approaches 1, the outflow jets develop a more focussed, narrow shape. The inviscid situation for the case $\beta = 0.8$ is illustrated in figure 8. Here, the predictions of the linearized theory in § 3 are drawn with dashed lines at the three different times $t = 4$, 8 and 12. The nonlinear inviscid interface $r = \mathscr{R}(\phi, t)$ calculated from § 2 at the same three times is overlaid, using heavier solid lines. The

https://doi.org/10.1017/jfm.2016.9 Published online by Cambridge University Press

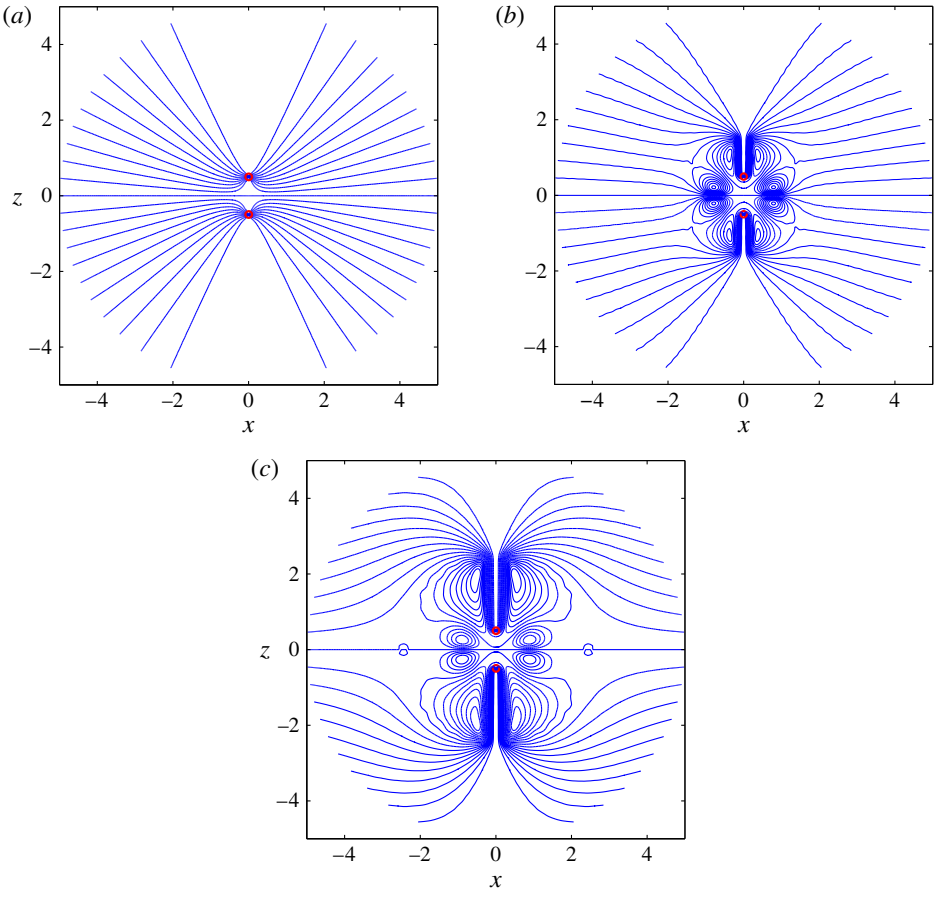


FIGURE 7. (Colour online) Evolution of streamlines in the viscous model at the three times (*a*) $t=4$, (*b*) $t=10$ and (*c*) $t=13$. The source location parameter is $\beta=0.5$ and the two sources have strengths $\eta_1=\eta_2=0.1$. The two masses are equal, so $\gamma=1$. The two small circles on the z-axis at $z=\pm 0.5$ (red online) give the source locations.

agreement between the two theories is reasonably good over much of the interface, at all three times shown, except near the top and bottom poles of the original sphere, where the linearized theory very strongly overestimates the extent of the outflow, at least in the context of the inviscid model. It turns out, however, that the nonlinear viscous model also produces elongated outflow jets near the two poles, although they are much sharper and more focussed that the inviscid linearized solutions in figure 8. The viscous predictions are now investigated in figure 9.

The outflow for two equal sources of strength $\eta_1=\eta_2=0.1$ and source location parameter $\beta=0.8$ is shown for the viscous case in figure 9, at the three different times $t=4$, 8 and 12. After this time, the numerical algorithm of § 4 could not continue further. The scales on these axes are all equal, so that the shapes are as they would actually be seen, and each diagram has been drawn to the same size, so that they can be viewed relative to one another. Each picture has been created from a contour map of the density perturbation function $\bar{\rho}$ by locating the contour $\bar{\rho}=0.02$ and then rotating it about the z-axis.

https://doi.org/10.1017/jfm.2016.9 Published online by Cambridge University Press

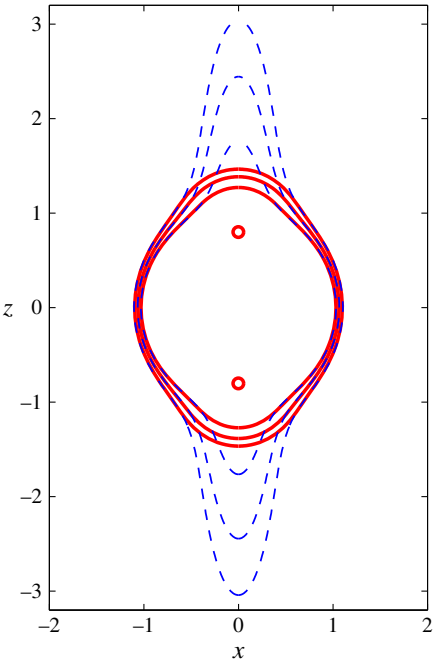


FIGURE 8. (Colour online) A comparison of the growth of the interface in the inviscid model, for the linearized (dashed; blue online) and nonlinear (heavy solid line; red online) theories. Solutions are shown at the three different times $t = 4$, 8 and 12. The source location parameter is $\beta = 0.8$ and their strengths are $\eta_1 = \eta_2 = 0.1$. The two masses are equal, so $\gamma = 1$. The two small circles (red online) give the source locations.

At the somewhat early time $t = 4$ in figure 9(*a*), the shape is still largely spherical of approximately unit radius, although outflow nodules have already begun to form at the poles, above the two point sources. By time $t = 8$, shown in figure 8(*b*), those nodules have developed into pronounced outflow jets, symmetrical about the equatorial plane $z = 0$. They possess small secondary waves, associated with the presence of vortices surrounding the jets, similar to those seen in figure 7(*c*). At the last time $t = 12$ shown in figure 9(*c*), the bipolar outflow jets have now developed further, forming long thin pencil-like jets with secondary wavelets. The central sphere-shaped region has actually decreased slightly in volume, as more fluid is pushed out to the rapidly expanding jets. Computing such structures is a challenge for a numerical technique, and solutions for t significantly larger than 12 have not been computed. Thus the ultimate fate of this solution for very large time remains unknown, but it is possible that the central spherical region may continue to shrink, and that the jets might become unstable and detach from it, and the whole cycle start again. At present, these fascinating morphological questions remain unanswered.

It is of interest now to see the effects of asymmetry on these outflows from two sources, in the viscous model. This could be achieved by replacing one of the sources with a sink, as in the inviscid case presented in figure 3, but in the viscous case the withdrawal of the finite-width interfacial zone into the sink is difficult to resolve, and so is not pursued here. Similarly, the two masses could be made unequal, so that $\gamma \neq 1$, but it turns out that this makes only slight changes to the results, and is likewise not discussed further here, in the interests of space. By far the most interesting situation is

https://doi.org/10.1017/jfm.2016.9 Published online by Cambridge University Press

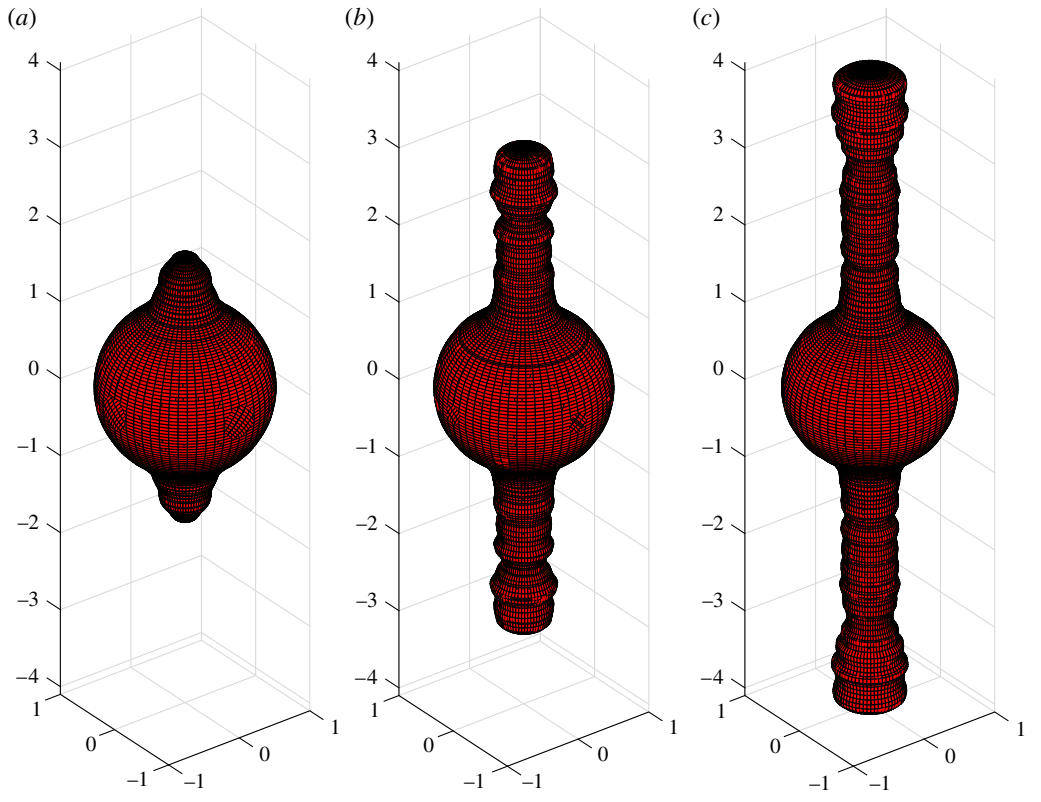


FIGURE 9. (Colour online) Perspective view of the evolution of the interface for the viscous solution at the three times (*a*) $t=4$, (*b*) $t=8$ and (*c*) $t=12$. The source location parameter is $\beta=0.8$ and the two sources have strengths $\eta_1=\eta_2=0.1$. The two masses are equal, so $\gamma=1$.

that in which one of the sources is much stronger than the other, since much greater asymmetry is produced in this case, as is perhaps to be expected. Such a situation is illustrated for the inviscid model in figure 10. Here, the upper source on the diagram still has strength $\eta_1=0.1$ but the lower source now has $\eta_2=0.3$. As for the symmetric cases shown in figures 2 and 8, the linearized solution very significantly overestimates the extent of the inviscid outflow near the sources, although it agrees very closely with the nonlinear result elsewhere along the interface. This is particularly evident near the lower, stronger, source in figure 10, where the pronounced bulge predicted by the linearized solution is not matched by the fully nonlinear inviscid result.

The predictions of the nonlinear viscous model are shown in figure 11, for the same parameters as the inviscid solution shown in previous figure 10, and for the same three times $t=1$, 2 and 3. The scale on the axes in the three pictures is the same, and each diagram has been drawn to be of the same size, to enable comparison. The three pictures were drawn by extracting the contour $\bar{\rho}=0.02$ from maps of the density perturbation function $\bar{\rho}(r,\phi,t)$ at the three times, and then revolving that contour about the z-axis. Once again, the upper source in these pictures has strength $\eta_1=0.1$ but the lower source is three times that strength, with $\eta_2=0.3$. The effect of this asymmetry in source strengths has an intriguing effect on the evolution of the outflow shape, as can be seen in figure 11. Now an essentially one-sided outflow is

https://doi.org/10.1017/jfm.2016.9 Published online by Cambridge University Press

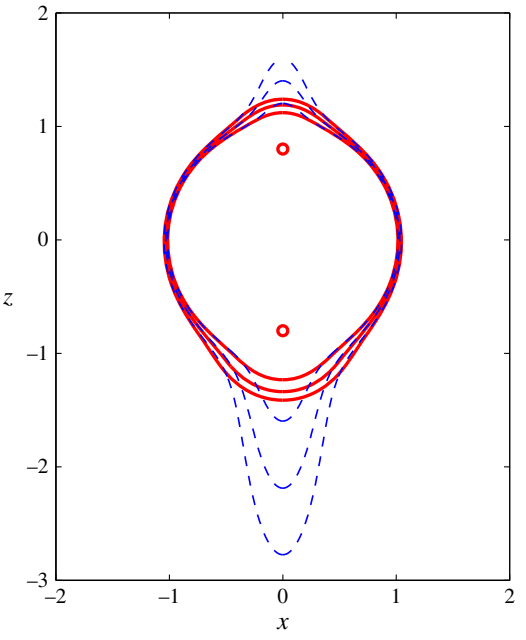


FIGURE 10. (Colour online) A comparison of the growth of the interface in the inviscid model, for the linearized (dashed; blue online) and nonlinear (heavy solid line; red online) theories. Solutions are shown at the three different times $t = 1$, 2 and 3. The source location parameter is $\beta = 0.8$ and the strengths are unequal, with $\eta_1 = 0.1$ and $\eta_2 = 0.3$. The two masses are equal, so $\gamma = 1$. The two small circles (red online) give the source locations.

generated, and looks at least superficially similar to the one-sided outflows produced by a single point source, discussed in Forbes (2011*b*), although the underlying reason for that shape in this case is very different.

At the early time $t = 1$ depicted in figure 11(*a*), the outflow shape is almost just the initial sphere of unit radius, except that a small bump is present at the bottom of the 'interfacial' surface $\bar{\rho} = 0.02$ below the lower source. At the later time $t = 2$ in figure 11(*b*), that bump has now developed into a pronounced outflow jet towards the bottom of the picture. In fact, the contour $\bar{\rho} = 0.02$ has actually pinched off to form a separate disconnected little surface at the bottom of the jet, although this may not be evident from figure 11(*b*). As time continues, the single jet grows longer and the final picture in figure 11(*c*) at the last time $t = 3$ now features a very long jet with a somewhat complicated shape that contains a number of smaller cylindrical waves around its axis. Indeed, the bottom three ripples visible at the end of the jet in figure 11(*c*) for the contour $\bar{\rho} = 0.02$ have all detached from the main jet and have had to be drawn separately, although this may again not be apparent from the diagram. Solutions for this case at later times have not been pursued, since the rapid development of the one-sided jet means that it is approaching the edge of the computational region, at the 'artificial boundary' $R = 5$. To continue much beyond this time would require very greatly increased computer resources, since this boundary would have to be moved further out, necessitating in turn far more Fourier modes in the spectral solution representations (4.11) and so on, and many more mesh points for the accurate evaluation of the integrals in the spectral solution technique. As

https://doi.org/10.1017/jfm.2016.9 Published online by Cambridge University Press

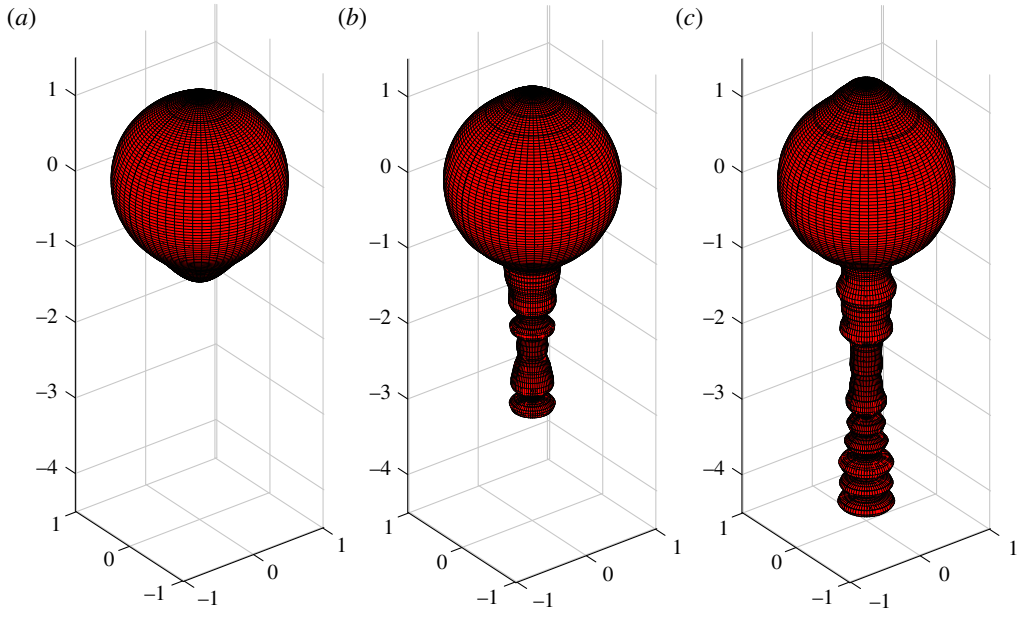


FIGURE 11. (Colour online) Perspective view of the evolution of the interface for the viscous solution at the three times (*a*) $t=1$, (*b*) $t=2$ and (*c*) $t=3$. The source location parameter is $\beta=0.8$ and the two sources have unequal strengths, with $\eta_1=0.1$ and $\eta_2=0.3$. The two masses are equal, so $\gamma=1$.

discussed in relation to figure 9 in the symmetrical case, the eventual fate of the one-sided outflow in figure 11 is likewise unknown at this time, although it is to be expected that the jet will continue to elongate, possibly with more and more detached segments as it does so.

6. Conclusion

When a single point source is placed in a surrounding fluid, and the source ejects fluid of a different density to its surroundings, the interface between the two fluids has been found to be unstable to the lowest mode, in axisymmetric geometry. This was shown earlier by Forbes (2011*b*), and the practical consequence is that a one-sided outflow jet is the most likely result. This is a surprising conclusion, and is not matched in the two-dimensional flow situation in which a line source ejects less dense fluid into a more dense medium (Forbes 2011*a*). Nevertheless, one-sided ejecta have been observed in astrophysics by Gómez *et al.* (2013) and are also reported in computational astrophysics, when an artificial constraint of symmetry about the centre plane is not imposed (Lovelace *et al.* 2014).

Since bipolar outflows are often observed in astrophysics, for example (see Stahler & Palla 2004), it is natural to ask whether such structures might be produced by a binary pair of sources, and this has been the focus of the present research. Inviscid theory shows that, when the two sources are of identical mass and strength, a genuinely symmetrical outflow is indeed produced. A linearized solution has been presented in the inviscid case, and it agrees well with the nonlinear inviscid results, except near the regions of the two outflows, where it tends to exaggerate the size of the outflow region. Interestingly, when viscosity is introduced into the model,

https://doi.org/10.1017/jfm.2016.9 Published online by Cambridge University Press

through a Boussinesq approximation, it is found that the outflow regions are in fact much more pronounced than the nonlinear inviscid theory allows; in that regard they are superficially similar to the linearized inviscid theory, although their structure is quite different. In addition, sources of very different strength can produce one-sided outflows, as shown in figure 11, and this may have relevance to the findings of Murphy *et al.* (2008).

The introduction of a second source within the region of the less dense fluid poses new numerical challenges. These have been addressed in this paper by the use of a novel spectral method in which the perturbation to the fluid density is made to vanish exactly at the two sources, so enforcing exactly the correct value of the density at those two points. This has only a minor effect on the buoyancy term in the vorticity (4.3), but it means that the basis functions in the spectral method are no longer orthogonal when applied to the density transport equation in the system (4.4). However, this difficulty is overcome here by storing the inverse of a matrix of the inner products of the basis functions, once at the beginning of the numerical algorithms, and then using it at each time step to integrate the density perturbation forward in time. Consequently, the computational cost of using such non-orthogonal basis functions is minimized. No difficulty has been encountered in this work with issues of ill conditioning that might arise from the non-orthogonality of the basis functions in the representation (4.11), (4.13) for density, with the two sources studied here. In principle, this new approach could be adapted to account for any number of sources within the fluid, although it may be that additional sources could indeed introduce numerical ill conditioning in the corresponding representation for density.

While the motivation for the present study has notionally involved astrophysical applications, it is nevertheless the case that this represents a canonical problem in fundamental fluid mechanics. It could, therefore, equally well apply to underwater explosions or inflows to reservoirs, for example. It should be possible to generalize such a study to account for additional effects such as magnetic forces or perhaps compressibility, as well as the influence of additional sources, and these are currently under investigation.

Acknowledgements

This work has been carried out in association with ARC (Australian Research Council) discovery grant DP140100094. I am indebted to Dr S. Walters for assistance with some of the figures. Constructive comments from three anonymous referees are gratefully acknowledged.

Appendix A. Differential equations for Boussinesq Fourier coefficients

The vorticity (4.3) is subject to Fourier decomposition, as detailed in § 4. This results in a system of equations for the time derivatives of the coefficients $A_{mn}(t)$. After some algebra, that system is

$$\begin{aligned} A'_{k\ell}(t) \;=\; & -\frac{1}{R_e}\alpha_{\ell k}^2 A_{k\ell}(t) \\ & -\frac{1}{\Delta_{k\ell}}\int_0^R\int_0^\pi \sqrt{r}\left[ru\frac{\partial\zeta_\theta}{\partial r}+w\frac{\partial\zeta_\theta}{\partial\phi}\right]\mathrm{J}_{\ell+1/2}(\alpha_{\ell k}r)P'_\ell(\cos\phi)\sin^2\phi\,\mathrm{d}\phi\,\mathrm{d}r \\ & +\frac{1}{\Delta_{k\ell}}\int_0^R\int_0^\pi \sqrt{r}\zeta_\theta[u\sin\phi+w\cos\phi]\mathrm{J}_{\ell+1/2}(\alpha_{\ell k}r)P'_\ell(\cos\phi)\sin\phi\,\mathrm{d}\phi\,\mathrm{d}r \end{aligned}$$

https://doi.org/10.1017/jfm.2016.9 Published online by Cambridge University Press

$$+\frac{1}{F_1^2\Delta_{k\ell}}\int_0^R\int_0^\pi \sqrt{r}\frac{\mathscr{G}_M}{Z_M^{3/2}}\mathrm{J}_{\ell+1/2}(\alpha_{\ell k}r)P'_\ell(\cos\phi)\sin^2\phi\,\mathrm{d}\phi\,\mathrm{d}r$$
$$+\frac{\gamma}{F_1^2\Delta_{k\ell}}\int_0^R\int_0^\pi \sqrt{r}\frac{\mathscr{G}_P}{Z_P^{3/2}}\mathrm{J}_{\ell+1/2}(\alpha_{\ell k}r)P'_\ell(\cos\phi)\sin^2\phi\,\mathrm{d}\phi\,\mathrm{d}r,$$
$$k=1,\ldots,M,\ \ell=1,\ldots,N, \tag{A 1}$$

where

$$\mathscr{G}_M(r,\phi,t)=(r-\beta\cos\phi)\frac{\partial\bar\rho}{\partial\phi}-\beta r\sin\phi\frac{\partial\bar\rho}{\partial r}, \tag{A 2}$$

$$\mathscr{G}_P(r,\phi,t)=(r+\beta\cos\phi)\frac{\partial\bar\rho}{\partial\phi}+\beta r\sin\phi\frac{\partial\bar\rho}{\partial r}. \tag{A 3}$$

The constants $\Delta_{k\ell}$ in (A 1) come from the orthogonality relations for the derivatives of the Legendre polynomials and for the Bessel functions, and are defined to be

$$\Delta_{k\ell}=R^2\alpha_{\ell k}^2\mathrm{J}_{\ell+3/2}^2(\alpha_{\ell k}R)\frac{\ell(\ell+1)}{(2\ell+1)}. \tag{A 4}$$

There are also two functions in (A 1) that arise from the function defined in (4.13); these are

$$\left.\begin{aligned}Z_M(r,\phi)&=r^2-2\beta r\cos\phi+\beta^2,\\ Z_P(r,\phi)&=r^2+2\beta r\cos\phi+\beta^2,\end{aligned}\right\} \tag{A 5}$$

and these are chosen to vanish at the upper and lower source points, respectively.

A further set of differential equations (4.15), (4.17) is obtained after Fourier decomposition of the density transport equation, as detailed in § 4. These expressions involve a large number of intermediate constants, expressed as integrals. In (4.15), these constants are

$$\mathscr{M}_{m0k0}=\int_0^R\int_0^\pi \mathscr{H}\cos(\alpha_{0m}r)\cos(\alpha_{0k}r)\sin\phi\,\mathrm{d}\phi\,\mathrm{d}r, \tag{A 6a}$$

$$\mathscr{N}_{mnk0}=\int_0^R\int_0^\pi \mathscr{H}\frac{1}{\sqrt{r}}\mathrm{J}_{n+1/2}(\alpha_{nm}r)P_n(\cos\phi)\cos(\alpha_{0k}r)\sin\phi\,\mathrm{d}\phi\,\mathrm{d}r, \tag{A 6b}$$

$$R_{k0}=\int_0^R\int_0^\pi\left[-\frac{1}{(D-1)}\left(u\frac{\partial\bar\rho}{\partial r}+\frac{w}{r}\frac{\partial\bar\rho}{\partial\phi}\right)+\sigma\mathscr{L}_D\right]\cos(\alpha_{0k}r)\sin\phi\,\mathrm{d}\phi\,\mathrm{d}r. \tag{A 6c}$$

In the last of these quantities, the symbol $\mathscr{L}_D$ represents the Laplacian of the function $\bar\rho$ in (4.11), but is not given here in the interests of space. The similar constants arising from (4.17) are

$$\mathscr{M}_{m0k\ell}=\int_0^R\int_0^\pi \mathscr{H}r^{3/2}\mathrm{J}_{\ell+1/2}(\alpha_{\ell k}r)\cos(\alpha_{0m}r)P_\ell(\cos\phi)\sin\phi\,\mathrm{d}\phi\,\mathrm{d}r, \tag{A 7a}$$

$$\mathscr{N}_{mnk\ell}=\int_0^R\int_0^\pi \mathscr{H}r\mathrm{J}_{n+1/2}(\alpha_{nm}r)\mathrm{J}_{\ell+1/2}(\alpha_{\ell k}r)P_n(\cos\phi)P_\ell(\cos\phi)\sin\phi\,\mathrm{d}\phi\,\mathrm{d}r, \tag{A 7b}$$

$$R_{k\ell}=\int_0^R\int_0^\pi\left[-\frac{1}{(D-1)}\left(u\frac{\partial\bar\rho}{\partial r}+\frac{w}{r}\frac{\partial\bar\rho}{\partial\phi}\right)+\sigma\mathscr{L}_D\right]\times r^{3/2}\mathrm{J}_{\ell+1/2}(\alpha_{\ell k}r)P_\ell(\cos\phi)\sin\phi\,\mathrm{d}\phi\,\mathrm{d}r. \tag{A 7c}$$

https://doi.org/10.1017/jfm.2016.9 Published online by Cambridge University Press

REFERENCES

ABRAMOWITZ, M. & STEGUN, I. A. (Eds) 1972 *Handbook of Mathematical Functions*. Dover.

BATCHELOR, G. K. 1967 *An Introduction to Fluid Dynamics*. Cambridge University Press.

CHENÉ, A.-N. & ST-LOUIS, N. 2010 Large-scale periodic variability of the wind of the Wolf–Rayet star WR 1 (HD 4004). *Astrophys. J.* **716**, 929–941.

CLEMENTEL, N., MADURA, T. I., KRUIP, C. J. H. & PAARDEKOOPER, J.-P. 2015 3D radiative transfer simulations of Eta Carinae's inner colliding winds – II. Ionization structure of helium at periastron. *Mon. Not. R. Astron. Soc.* **450**, 1388–1398.

DAVIDSON, K. & HUMPHREYS, R. M. 1997 Eta Carinae and its environment. *Annu. Rev. Astron. Astrophys.* **35**, 1–32.

EPSTEIN, R. 2004 On the Bell–Plesset effects: the effects of uniform compression and geometrical convergence on the classical Rayleigh–Taylor instability. *Phys. Plasmas* **11**, 5114–5124.

FORBES, L. K. 2009 The Rayleigh–Taylor instability for inviscid and viscous fluids. *J. Engng Maths* **65**, 273–290.

FORBES, L. K. 2011*a* A cylindrical Rayleigh–Taylor instability: radial outflow from pipes or stars. *J. Engng Maths* **70**, 205–224.

FORBES, L. K. 2011*b* Rayleigh–Taylor instabilities in axi-symmetric outflow from a point source. *ANZIAM J.* **53**, 87–121.

FORBES, L. K. 2014*a* How strain and spin may make a star bipolar. *J. Fluid Mech.* **746**, 332–367.

FORBES, L. K. 2014*b* Planar Rayleigh–Taylor instabilities: outflows from a binary line-source system. *J. Engng Maths* **89**, 73–99.

FORBES, L. K. & BRIDESON, M. A. 2014 Exact solutions for interfacial outflows with straining. *ANZIAM J.* **55**, 232–244.

FORBES, L. K., CHEN, M. J. & TRENHAM, C. E. 2007 Computing unstable periodic waves at the interface of two inviscid fluids in uniform vertical flow. *J. Comput. Phys.* **221**, 269–287.

FORBES, L. K. & HOCKING, G. C. 2007 Unsteady draining flows from a rectangular tank. *Phys. Fluids* **19**, 082104,1–14.

FORBES, L. K., PAUL, R. A., CHEN, M. J. & HORSLEY, D. E. 2015 Kelvin–Helmholtz creeping flow at the interface between two viscous fluids. *ANZIAM J.* **56**, 317–358.

FORBRICH, J., STANKE, TH., KLEIN, R., HENNING, TH., MENTEN, K. M., SCHREYER, K. & POSSELT, B. 2009 A multi-wavelength study of a double intermediate-mass protostar – from large-scale structure to collimated jets. *Astron. Astrophys.* **493**, 547–556.

FRANCO-HERNÁNDEZ, R. & RODRÍGUEZ, L. F. 2003 VLA detection of a double radio source at the center of the HH 288 quadrupolar outflow. *Rev. Mex. Astron. Astrofis.* **39**, 107–111.

GÓMEZ, L., RODRÍGUEZ, L. F. & LOINARD, L. 2013 A one-sided knot ejection at the core of the HH 111 outflow. *Rev. Mex. Astron. Astrofis.* **49**, 79–85.

GRADSHTEYN, I. S. & RYZHIK, I. M. 2000 *Tables of Integrals, Series and Products*, 6th edn. Academic.

HOCKING, G. C. 1995 Supercritical withdrawal from a 2-layer fluid through a line sink. *J. Fluid Mech.* **297**, 37–47.

KREYSZIG, E. 2011 *Advanced Engineering Mathematics*, 10th edn. Wiley.

LADD, E. F. & HODAPP, K.-W. 1997 A double outflow from a deeply embedded source in Cepheus. *Astrophys. J.* **475**, 749–759.

LOVELACE, R. V. E., ROMANOVA, M. M., LII, P. & DYDA, S. 2014 On the origin of jets from disc-accreting magnetized stars. *Comput. Astrophys. Cosmol.* **1**, 10pp. http://www.comp-astrophys-cosmol.com/content/1/1/3.

LOVELACE, R. V. E., ROMANOVA, M. M., USTYUGOVA, G. V. & KOLDOBA, A. V. 2010 One-sided outflows/jets from rotating stars with complex magnetic fields. *Mon. Not. R. Astron. Soc.* **408**, 2083–2091.

MADURA, T. I., CLEMENTEL, N., GULL, T. R., KRUIP, C. J. H. & PAARDEKOOPER, J.-P. 2015 3D printing meets computational astrophysics: deciphering the structure of η Carinae's inner colliding winds. *Mon. Not. R. Astron. Soc.* **449**, 3780–3794.

MATSUOKA, C. & NISHIHARA, K. 2006 Analytical and numerical study on a vortex sheet in incompressible Richtmyer–Meshkov instability in cylindrical geometry. *Phys. Rev.* E **74**, 066303,1–12.

https://doi.org/10.1017/jfm.2016.9 Published online by Cambridge University Press

MIKAELIAN, K. O. 2005 Rayleigh–Taylor and Richtmyer–Meshkov instabilities and mixing in stratified cylindrical shells. *Phys. Fluids* **17**, 094105,1–13.

MOORE, D. W. 1979 The spontaneous appearance of a singularity in the shape of an evolving vortex sheet. *Proc. R. Soc. Lond.* A **365**, 105–119.

MURPHY, G. C., LERY, T., O'SULLIVAN, S., SPICER, D., BACCIOTTI, F. & ROSEN, A. 2008 Interacting jets from binary protostars. *Astron. Astrophys.* **478**, 453–460.

NASA, 2015 NASA Observatories take an unprecedented look into superstar Eta Carinae. https://www.nasa.gov/content/goddard/nasa-observatories-take-an-unprecedented-look-into-superstar-eta-carinae.

PEREGRINE, D. H. 1972, A line source beneath a free surface. Rep. no. 1248. University of Wisconsin Mathematics Research Center.

SMITH, N. 2013 A model for the 19th century eruption of Eta Carinae: CSM interaction like a scaled-down Type IIn Supernova. *Mon. Not. R. Astron. Soc.* **429**, 2366–2379.

STAHLER, S. W. & PALLA, F. 2004 *The Formation of Stars*. Wiley-VCH.

STEFFEN, W., TEODORO, M., MADURA, T. I., GROH, J. H., GULL, T. R., MEHNER, A., CORCORAN, M. F., DAMINELI, A. & HAMAGUCHI, K. 2014 The three-dimensional structure of the Eta Carinae Homunculus. *Mon. Not. R. Astron. Soc.* **442**, 3316–3328.

STOKES, T. E., HOCKING, G. C. & FORBES, L. K. 2003 Unsteady free-surface flow induced by a line sink. *J. Engng Maths* **47**, 137–160.

TUCK, E. O. & VANDEN-BROECK, J.-M. 1984 A cusp-like free-surface flow due to a submerged source or sink. *J. Austral. Math. Soc.* B **25**, 443–450.

ULVESTAD, J. S., WROBEL, J. M. & CARILLI, C. L. 1999 Radio continuum evidence for outflow and absorption in the Seyfert 1 Galaxy Markarian 231. *Astrophys. J.* **516**, 127–140.

VANDEN-BROECK, J.-M., SCHWARTZ, L. W. & TUCK, E. O. 1978 Divergent low-Froude-number series expansion of non-linear free-surface flow problems. *Proc. R. Soc Lond.* A **361**, 207–224.

VON WINCKEL, G. 2004 *lgwt.m*. at: MATLAB file exchange website. http://www.mathworks.com/matlabcentral/fileexchange/loadFile.do?objectId=4540&objectType=file.

XUE, M. & YUE, D. K. P. 1998 Nonlinear free-surface flow due to an impulsively started submerged point sink. *J. Fluid Mech.* **364**, 325–347.

ZINNECKER, H. & YORKE, H. W. 2007 Toward understanding massive star formation. *Annu. Rev. Astron. Astrophys.* **45**, 481–563.

https://doi.org/10.1017/jfm.2016.9 Published online by Cambridge University Press